

2

DTIC COPY

AD-A217 993

NUMERICAL MODELING OF AIRBLAST
3RD YEAR ANNUAL REPORT

SAIC 89/1732
November 1989



Science Applications International Corporation
An Employee-Owned Company

DTIC
ELECTE
FEB 20 1990
S D D
D

DISTRIBUTION STATEMENT A
Approved for public release
Distribution Unlimited

90 02 15 001

2

**NUMERICAL MODELING OF AIRBLAST
3RD YEAR ANNUAL REPORT**

**SAIC 89/1732
November 1989**



Science Applications International Corporation
An Employee-Owned Company

DTIC
ELECTE
FEB 20 1990
S D

DISTRIBUTION STATEMENT A
Approved for public release
Distribution Unlimited

NUMERICAL MODELING OF AIRBLAST

3RD YEAR ANNUAL REPORT

SAIC 89/1732

November 1989

Submitted to:

Dr. William Sandberg
Deputy Director
Laboratory for Computational Physics
and Fluid Dynamics
Naval Research Laboratory
Washington, DC 20375-5000

Prepared by:

Dr. Ellis Hyman
with
Dr. Richard Leighton, Dr. Ravi Ramamurti, and Mr. Mike Zuniga

Prepared under:

Contract No. N00014-86-C-2197

For the Period from March 10, 1988
to September 9, 1989

TABLE OF CONTENTS

I.	Discussion	1
II.	Numerical Simulation of Turbulent Flow at a Free-Surface	1
III.	Simulation of Inviscid/Viscous Flows Over Complex Geometries	4
IV.	Algorithm Development for Multitarget Tracking.....	5

STATEMENT "A" per Dr. W. Sandberg
 NRL/Code 4401
 TELECON

2/20/90

CG



Accession For	
NTIS CRA&I	<input checked="" type="checkbox"/>
DTIC TAB	<input type="checkbox"/>
Unannounced	<input type="checkbox"/>
Justification	
By <i>per call</i>	
Distribution/	
Availability Codes	
Dist	Avail and/or Special
<i>A-1</i>	

I DISCUSSION

We describe the SAIC accomplishments for the final contract period. Our previous annual report for this contract, N00014-86-C-2147, described the work performed up to March 9, 1988. Here the period covered is March 10, 1988 to September 9, 1989. Because of budget considerations the scale of our program was cut back and the research performed was undertaken after consultations with the COTR for the Laboratory for Computational Physics and Fluid Dynamics (LCPFD) of the Naval Research Laboratory (NRL).

The accomplishments of the program cover three major areas. They include the development of computer codes to numerically simulate (1) turbulent flow at a free-surface and (2) inviscid/viscous flows over complex geometries. The third area concerns the development of numerical algorithms for multitarget tracking. (LCP) (←)

II. NUMERICAL SIMULATION OF TURBULENT FLOW AT A FREE-SURFACE

Introduction

Much of this year's effort was directed at performing a direct numerical simulation of turbulent flow at a free-surface. There were several distinct steps taken in this direction and several distinct physical problems examined. All of the work discussed below was performed at NRL in collaboration with Drs. T. Swain, R. Handler, and H. Wang of NRL.

Development of Fast Poisson Solvers Using a Pseudo-Spectral Algorithm

At the center of any Navier-Stokes solver using pseudo-spectral methods are Poisson solvers and Fast Fourier Transforms (FFT). For the Fourier transforms, the latest version of the FFTs from Cray Research Inc. were used. For the Poisson solvers, we implemented an algorithm described by Orszag and Gottlieb (1977) and optimized it for the Cray X-MP at NRL. These Poisson solvers allow a single non-homogeneous direction and a single homogeneous direction. Chebechev polynomials are used as expansion functions in the non-homogeneous direction and trigonometric functions in the homogeneous direction. In the non-homogeneous direction Neumann, Dirichlet or Robin¹ boundary conditions can be used.

Development of a Two Dimensional Navier-Stokes Solver

A two dimensional Navier-Stokes solver was developed as a test bed for the numerical algorithm. The governing Navier-Stokes equations are recast into a 4th order equation for the vertical velocity and a 2nd order equation for the vertical vorticity and the continuity equation is solved explicitly in the recovery of the streamwise velocity. The equations are numerically solved after they are Fourier transformed in the streamwise (x) and spanwise (z) directions and Chebychev transformed in the vertical direction (y). For a two dimensional simulation the spanwise direction and the equation for vertical vorticity are omitted.

Additionally, an Orr-Sommerfeld solver was developed to determine initial conditions for the simulations. Solutions to the Orr-Sommerfeld equations with the model free-surface boundary conditions indicated that the open channel, free-surface two dimensional flow is always stable in the parameter range that we considered. Using the Navier-Stokes solver, a direct simulation indicated that the flow is also stable to finite amplitude perturbations.

The Navier-Stokes solver is also being used to perform direct numerical simulations of a vortex pair interacting with the free-surface. In this work, done in collaboration with Henry Wang, a velocity field vortex pair is specified as an initial condition and allowed to propagate to the free-surface. The model free-surface boundary condition was modified to include the effects of a surface contaminant. The addition of a surface contaminant imposed a flow dependent stress on the free-surface. This work is described in more detail in Appendix A, which will appear in the 9th International Conference on Offshore Mechanics and Arctic Engineering, February 18-25, 1990.

Development of a Three Dimensional Navier Stokes Solver

The two dimensional Navier-Stokes solver was converted into a three dimensional solver by the addition of the equation for vertical vorticity. A strong emphasis was placed on both the computational speed, or efficiency, of the computer code and its versatility in terms of the application of boundary conditions. The program runs at 40 percent of the theoretical speed of the Cray X-MP. The code was developed to allow both slip and no

slip boundary conditions and either zero normal velocity or a specified normal velocity (blowing or sucking boundaries in the parlance of turbulence research). Much of the effort of the current year will be directed towards developing new boundary conditions.

Analysis of Free-Surface Turbulent Flow

The incompressible three-dimensional Navier-Stokes equations are solved for initial and boundary conditions approximating a turbulent open-channel flow of water at $Re_h = 3000$ where h is the channel depth. Most of the calculations were performed on a $32 \times 65 \times 64$ grid in x, y, z respectively. This resolution allows six grid points to occur within the viscous sublayer. In the spanwise and streamwise directions, the grid spacing is approximately $0.1h$ and $0.2h$ respectively. These should be compared to the physically relevant scales of the low speed streaks in the wall region: $1h$ and $5h$, respectively at this Reynolds number. All essential turbulent scales needed for the determination of most statistical and flow structure properties have been resolved, as can be determined by comparison to relevant experimental and numerical results. A subgrid or large eddy model has not been used. The boundary conditions are periodic in all dependent variables in the streamwise and span-wise directions. No slip conditions are used at the channel bottom while the free surface is approximated as a rigid free slip surface with vanishing shear.

A large number of turbulence statistics are computed in the vicinity of the free surface and complete determinations of the balances of the exact Reynolds stress, turbulence kinetic energy, and isotropic dissipation rate equations are reported for the first time. The results show that while the turbulence kinetic energy is preserved in the vicinity of the free surface, the turbulence is redistributed from the vertical component into the two horizontal components. The vertical vorticity at the free surface is concentrated in regions elongated in the streamwise direction. This anisotropic behavior leads to preferential redistribution of the turbulence kinetic energy into the span-wise component of kinetic energy. The balances of the streamwise and span-wise components of the turbulence kinetic energy reveal a reversal in sign of the pressure-velocity correlations in this region. A physical model has been suggested to explain this behavior. It is apparent from the kinetic energy and dissipation balances that there

exist two separate regions near the free surface, a thin viscous layer and a thicker zone wherein the redistribution of turbulence is more pronounced. Near surface expansions of the turbulence kinetic energy and isotropic dissipation rate are determined for use in Reynolds-averaged turbulence models. A paper describing this work is in preparation and will be submitted for publication.

III. SIMULATION OF INVISCID/VISCOUS FLOWS OVER COMPLEX GEOMETRIES

The use of unstructured grids for the simulation of high-speed flows can be found in the literature (see references cited in the appendices). In the present research effort, we have extended this technology to nearly incompressible flows, and applied the procedure to simulate inviscid as well as viscous flows past submarine configurations with all its appendages. One attractive feature of using triangular or tetrahedral meshes over structured meshes is that complex geometries can be easily represented. For example, constructing a structured mesh around a submarine with all its appendages will require a tedious task of decomposition of the domain. In the present work, unstructured grids are generated using the advancing front algorithm of Lohner. The governing equations of flow are solved using the finite-element version of the Flux-Corrected Transport algorithm (FEM-FCT). Details of the flow solver can be found in the appendices referred to in this section.

As a first step, Euler and Navier-Stokes solutions were obtained for axisymmetric flows. This provided an excellent case to validate the procedure employed and also a base to build models for predicting turbulent flows. The procedure was applied to solve a model problem of flow over a sphere and the computed results were found to be in good agreement with those found in the literature for both the potential flow case and the case of viscous flow at Reynolds-number, $Re = 100$. These are part of the paper submitted for publication in the IJNMFJ journal, which is included here as Appendix B. Having established the correctness of the procedure, it was then extended to compute flow over the submarine hull configuration. Grid refinement studies were conducted for the inviscid flow in order to establish the independence of the flow solution to the chosen grid. Also, a laminar viscous flow solution for this configuration was obtained for $Re =$

1000. The convergence rate for this problem deteriorated considerably, as would be expected, due to the presence of the small elements in the boundary layer which are needed to resolve the high gradients present in the flow variables. Hence, convergence acceleration of the numerical method was investigated by appropriately sub-stepping the viscous diffusion terms. It was found that this method of convergence acceleration did not yield substantial gain because the allowable time-step for the explicit scheme for low Mach numbers is limited by the speed of sound. For explicit schemes, the allowable time-step due to the advective terms is given by

$$\Delta t_{adv} \leq \frac{\Delta}{|u| c}$$

where Δ is the minimum cell size, u is velocity and c is the speed of sound. For low subsonic flows, the allowable Δt_{adv} therefore decreases. Hence, this convergence acceleration procedure should be investigated with the barely-implicit correction (BIC) scheme.

The procedure was next extended to solve three-dimensional flows. Results were obtained for inviscid flow over the submarine with sail and stern appendages at various pitch angles of attack. This work was presented at the APS meeting in November 1989, and an abstract of this presentation is included in this report as Appendix C. In order to predict the formation of vortices and hence the noise generated by them, it is important to carry out a Navier-Stokes analysis. Therefore, the viscous diffusion terms were incorporated into the 3-D version of the flow solver. In the numerical procedure, these terms were treated as a deferred correction in the second step of the Taylor-Galerkin procedure. Preliminary coarse grid results of the fully appended model at a pitch angle of attack of 10° show the presence of vortices at the junction of the sail and the hull and also at the tips of the stern planes. This configuration was also studied at a yaw angle of attack, in order to predict the forces and moments that will be involved in a maneuvering submarine. This effort will be presented at the AIAA 28th Aerospace Sciences Meeting and an extended abstract is attached as Appendix D.

IV. ALGORITHM DEVELOPMENT FOR MULTITARGET TRACKING

This section describes the SAIC effort in the application of advanced computer science algorithms for multitarget tracking. The effort starts with the notion that near neighbors finding algorithms can be used to help track objects, and it has evolved into the identification and solution of an important problem that occurs in state-of-the-art multitarget tracking algorithms.

The part of the tracking problem we have focused on is the combinatorial explosion that can occur in gating. The previous year annual report² gives an overview of tracking bottlenecks and it includes suggestions for efficiency improvements in the various parts, and in particular for gating. A recent SAIC report³ has detailed descriptions and test results of the algorithms we have devised for efficient gating performance. The results are encouraging. A copy of this report is included in Appendix E. In the following, we outline the essential results.

We have discovered that we can perform gating efficiently if we do three things: (1) use the characteristics of the Gaussian correlation measure to obtain a Euclidian search radius from values of the measure. This allows the use of efficient geometrical computational methods; and it is a breakthrough because the correlation measure is a function of report and track covariance distributions as well as on their position distributions. (2) Recognize that once you have a search radius you can use existing fast near-neighbors finding algorithms to pair the reports to the tracks. (3) In the case where the observation times of the reports are unequal, use an auxiliary algorithm that makes "multiple projections" of the search data structures and helps the near neighbors finding algorithms retain good overall scaling.

Applying these techniques takes us one significant step forward in having a correlator/tracker that can process very large numbers of objects, including SDI scenario numbers of objects, in real time. This is principally so because the algorithms used to do the gating are designed for optimal or near optimal scaling, and it can be seen from analysis and data presented in³ that they approach $N \ln N$ scaling.

REFERENCES

1. Karl Gustafson, "Introduction to Partial Differential Equations and Hilbert Space Methods," Wiley and Sons, New York, 1980.
2. E. Hyman, S. Eidelman, M. Zuniga, and M. Redmon, "Numerical Modeling of Airblast, Second Year Annual Report," SAIC Report No. 88/1779, 3 (1988).
3. Miquel R. Zuniga, "Algorithms for Improved Gating Combinatorics in Multitarget Tracking," SAIC Report No. 89/1519, 1989.

APPENDIX A

Direct Calculation of the Interaction Between Subsurface Vortices and
Surface Contaminant Distributions Using Spectral Methods

DIRECT CALCULATION OF THE INTERACTION BETWEEN SUBSURFACE VORTICES AND SURFACE CONTAMINANTS

Paper No. OMAE-90-332

H. T. Wang
Laboratory for Computational Physics and Fluid Dynamics
Naval Research Laboratory
Washington, D.C.

R. I. Leighton
Science Applications International Corporation
McLean, Virginia

ABSTRACT

This paper presents a numerical calculation of the evolution of the flow due to a pair of vortices rising toward a boundary surface. A spectral method, with transforms in Fourier-Chebyshev space, is used to solve the two-dimensional incompressible Navier-Stokes equations. Three conditions are considered at the surface: the fixed no-slip and shear-free conditions, and a novel variable shear condition due to the presence of a nonuniform contaminant distribution. An additional transport equation for the contaminant concentration is required in this case. The computation scheme is stable for low and moderate contaminant concentration gradient levels. Contour and line plots of the main and surface flows generally show the expected result that the variable shear case lies between the no-slip and shear-free cases.

INTRODUCTION

The use of vortex elements is a powerful and convenient method to model the velocity field in a fluid. These elements may take the form of points, blobs, sheets, or curved filaments. If bounding walls and fluid viscosity are neglected, the resulting fluid velocities are obtained by calculating the locations of the vortex elements, which move at the local velocity, and their induced velocities. Thus, the problem reduces largely to kinematics. In the case of a reflecting wall, the techniques of complex variables are often used to account for their presence. In the case of fluid viscosity, it is necessary to amend the calculation method to account for the diffusion of the vorticity as well as the creation of vorticity due to the no-slip condition at the wall. Leonard [1] and Saffman and Baker [2] have written earlier surveys of the various analytical and numerical vortex calculation methods while Sarpkaya [3] has written a more recent and comprehensive survey of these methods.

Methods which consider the basic equations of motion for the fluid are less often used to study vortex motions. These methods model more accurately the vortex generation at the bounding surfaces and the vortex diffusion at the expense of greater computational complexity. Examples of this type of approach are the studies of Ersoy and Walker [4] and Peace and Riley [5], who consider the case of a pair of counter rotating vortices approaching a bounding surface. In both studies, the flow field is initially divided into an inviscid outer flow and a viscous inner flow. In [4], the outer flow serves as a boundary condition for the boundary layer flow near a no-slip wall, while in [5] the outer flow

merely serves as the initial condition for the solution of the Navier-Stokes equations for a no-slip as well as a shear-free bounding surface. In both studies, finite differences are used to obtain the spatial derivatives.

In all of the above studies, the principal interest is in the vortex flow field away from the surface, which is taken to furnish fixed conditions. In aerodynamic applications, an important example of such a problem is the flow field above the runway due to the vortices left behind by departing or landing aircraft. In marine applications, it is of interest to ascertain the effect of the free surface on the performance of underwater lifting surfaces. More recently, improvements in remote sensing technology using such techniques as synthetic aperture radar and infrared radiometry make it of interest to ascertain the wake features around a surface or submerged marine vehicle. Thus, the experimental and theoretical determination of the surface elevation features of the wake due to submerged vortices is currently a field of active interest. Examples of experimental investigations are those of Sarpkaya [6] and Willmarth, Tryggvason, Hirska, and Yu [7], who study the surface wave features caused by the previously mentioned case of a pair of counter rotating vortices. Examples of numerical studies of this problem are those of Yu and Tryggvason [8] and Ohring and Lugt [9]. In [8], a potential flow combined vortex/boundary integral technique is used, while in [9] the Navier-Stokes equations are solved in curvilinear coordinates with finite differences used to calculate the spatial derivatives. As may be expected, the presence of the unknown free surface requires an iterative procedure at each time step.

In this paper, we present the results of a numerical investigation, using the Navier-Stokes equations, of the flow due to a pair of vortices approaching a free surface with an unknown boundary condition different from the wave elevation case considered in [8,9]. We use a spectral method, whereby the equations are solved in Fourier-Chebyshev transform space, instead of the previously used finite-difference methods. It is well known that the Chebyshev transform clusters the calculation points near the wall, where the flow gradients tend to be largest. In addition to the fixed no-slip and shear-free conditions at the surface, we consider the novel condition of shear due to the presence of an adsorbing surface contaminant, known also as a surfactant. In this case, the shear stress is variable and is a function of the constantly changing surfactant distribution on the surface. The modeling of this condition requires a transport equation for the surfactant distribution at

the surface and a coupling of the shear stress exerted by this contaminant into the boundary condition at the surface. Instead of using an iterative procedure due to the varying surface condition, we take advantage of our spectral approach to obtain a technique which gives results which are comparable in computer time to those for fixed conditions. This technique is, however, limited to low and moderate contaminant shear stress cases.

We start the body of the paper by describing the theoretical approach. This includes a description of the Navier-Stokes equations in rotational form, the derivation of the fourth-order formulation which implicitly satisfies the troublesome continuity condition, and the transformation of the resulting formulation into Fourier-Chebyshev space. We give the initial conditions for the vortex pair, and the dimensions of our computation domain. We describe next the transport equation for the surface contaminant, the computation technique, and its limitations. We then present contour plots of the velocity and vorticity distributions for the main flow for no-slip, shear-free, and contaminant surface conditions. We also present line plots of the evolution of the velocity, vorticity, and contaminant distributions on the surface for these same surface conditions. We conclude the paper by briefly summarizing the principal findings.

THEORETICAL APPROACH

Basic Equations

By using the initial vortex spacing a , the initial translational velocity of the vortex pair V_0 , and the fluid density ρ , as reference variables, the Navier-Stokes equations take the following dimensionless form

$$\frac{\partial \mathbf{u}}{\partial t} + \mathbf{u} \cdot \nabla \mathbf{u} = -\nabla p + \frac{1}{Re} \nabla^2 \mathbf{u} \quad (1)$$

where \mathbf{u} is the fluid velocity, t is the time, p is the pressure, $Re = \rho a V_0 / \mu$ is the Reynolds number, and μ is the fluid dynamic viscosity. For an incompressible fluid, the conservation of mass takes the form

$$\nabla \cdot \mathbf{u} = 0 \quad (2)$$

By using vector identities, Eq. (1) can be put in the following so-called rotational form

$$\frac{\partial \mathbf{u}}{\partial t} + \boldsymbol{\omega} \times \mathbf{u} = -\nabla P + \frac{1}{Re} \nabla^2 \mathbf{u} \quad (3)$$

where $P = p + \mathbf{u} \cdot \mathbf{u} / 2$ is the dynamic pressure head and $\boldsymbol{\omega} = \nabla \times \mathbf{u}$ is the vorticity. As noted by Hussaini and Zang [10], the use of this form in Fourier collocation methods, as in our study, conserves kinetic energy and hence tends to minimize the effect of nonlinear instabilities.

Handler, Hendricks, and Leighton [11] point out that a number of alternate methods may be used to advance Eqs. (2) and (3) in time. In coupled methods, the entire system is considered at a given time step. In splitting methods, the time step is split into a momentum step, and a step whereby the pressure is adjusted to satisfy the condition of incompressibility, Eq. (2). We use here an unsplit scheme, whereby the troublesome term involving P is eliminated and the incompressibility condition is implicitly satisfied by going to a higher fourth-order formulation. The approach implemented here is similar to that proposed by Kim, Moin, and Moser [12]. For the two-dimensional case considered here, this fourth-order equation may be derived as follows. First, write Eq. (3) in component form for the velocity u in the x -direction and the velocity v in the y -direction, where x and y are defined in Fig. 1. Then by taking $\partial^2 / \partial x^2$ of the equation for v and $-\partial^2 / \partial y \partial x$ of the equation

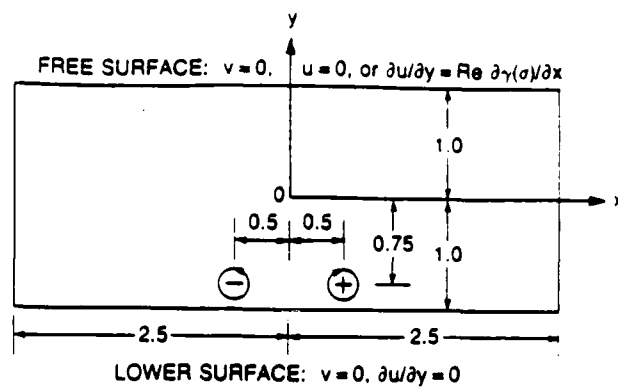


Fig. 1 — Definition of Initial Vortex Configuration and Computation Domain

for u , and using Eq. (2) to write $\partial u / \partial x$ as $-\partial v / \partial y$, the following fourth-order equation for v is obtained

$$\left(\frac{\partial}{\partial t} - \frac{1}{Re} \nabla^2 \right) \nabla^2 v = F \quad (4)$$

where F is the nonlinear term arising from $\boldsymbol{\omega} \times \mathbf{u}$, given by

$$F = -\frac{\partial^2(u\omega)}{\partial x^2} - \frac{\partial^2(v\omega)}{\partial y \partial x} \quad (5)$$

Numerical Solution Procedure

We advance Eq. (5) in time by using the weighted implicit Crank-Nicholson method for the linear term and the weighted explicit Adams-Bashforth method for the nonlinear term, resulting in the following equation for the value of v at the new $n+1$ time step in terms of values at the previous n and $n-1$ time steps

$$\begin{aligned} & \left(1 - \frac{\Delta t}{2Re} \nabla^2 \right) \nabla^2 v^{n+1} \\ & = \left[1 + \frac{\Delta t}{2Re} \nabla^2 \right] \nabla^2 v^n + \frac{\Delta t}{2} (3F^n - F^{n-1}) \end{aligned} \quad (6)$$

where Δt is the size of the time step. Since we assume the flow not to penetrate the upper and lower surfaces of our computation domain, shown in Fig. 1, the vertical velocity v is subject to the following boundary conditions

$$v = 0 \text{ on } y = \pm 1 \quad (7)$$

This means that both the upper and lower boundaries remain flat. We allow the horizontal velocity u and/or its derivative $\partial u / \partial y$ to be functions of x . Noting that $\partial u / \partial x = -(\partial v / \partial y)$ from continuity, Eq. (2), the boundary conditions on u take the following general form, expressed in terms of v

$$a_n \frac{\partial v}{\partial y} + b_n \frac{\partial^2 v}{\partial y^2} = c_n \text{ on } y = \pm 1 \quad (8)$$

where a_n and b_n are given constants and c_n are, in general, functions of x . Specializing the treatment given in [11] to the two-dimensional case, we proceed as follows to solve for v^{n+1} . We express v^{n+1} as the following sum of three partial solutions

$$v^{n+1} = v_p^{n+1} + \alpha^+ v_+^{n+1} + \alpha^- v_-^{n+1} \quad (9)$$

Each of the individual solutions satisfies the boundary condition given by Eq. (7), while the two boundary conditions given by Eq. (8) determine the unknown coefficients α^+ and α^- . To reduce the problem to second order we introduce the intermediate variable ζ which is related to v by

$$\zeta^{n+1} = \nabla^2 v^{n+1} \quad (10)$$

The formulation for the particular solution v_p which satisfies homogeneous boundary conditions but accounts for the nonlinear term F is given by

$$\left[1 - \frac{\Delta t}{2Re} \nabla^2 \right] \zeta_p^{n+1} = \left[1 + \frac{\Delta t}{2Re} \nabla^2 \right] \zeta^n + \frac{\Delta t}{2} (3F^n - F^{n-1}) \quad (11a)$$

$$\nabla^2 v_p^{n+1} = \zeta_p^{n+1} \quad (11b)$$

$$v_p^{n+1} = 0 \text{ on } y = \pm 1 \quad (11c)$$

$$\zeta_p^{n+1} = 0 \text{ on } y = \pm 1 \quad (11d)$$

The formulation for the solution v_+ which satisfies a nonzero boundary condition on $y = +1$ is given by

$$\left[1 - \frac{\Delta t}{2Re} \nabla^2 \right] \zeta_+^{n+1} = 0 \quad (12a)$$

$$\nabla^2 v_+^{n+1} = \zeta_+^{n+1} \quad (12b)$$

$$v_+^{n+1} = 0 \text{ on } y = \pm 1 \quad (12c)$$

$$\zeta_+^{n+1} = \begin{cases} 1, & \text{if } y = +1 \\ 0, & \text{if } y = -1 \end{cases} \quad (12d)$$

Finally, the formulation for the solution v_- which satisfies a nonzero boundary condition on $y = -1$ is given by

$$\left[1 - \frac{\Delta t}{2Re} \nabla^2 \right] \zeta_-^{n+1} = 0 \quad (13a)$$

$$\nabla^2 v_-^{n+1} = \zeta_-^{n+1} \quad (13b)$$

$$v_-^{n+1} = 0 \text{ on } y = \pm 1 \quad (13c)$$

$$\zeta_-^{n+1} = \begin{cases} 0, & \text{if } y = +1 \\ 1, & \text{if } y = -1 \end{cases} \quad (13d)$$

We note here that Eqs. (12) and (13) need be solved only once and give two solutions which may be regarded as independent Green functions whose coefficients α^+ and α^- are adjusted to satisfy the boundary conditions given in Eq. (8).

Transformation to Fourier-Chebyshev Space

In order to solve the above formulation in transform space, we expand $v(x, y, t)$ given in Eq. (9) as a series of exponential functions in the periodic x direction and Chebyshev polynomials in the y direction, as follows

$$v(x, y, t) = \sum_{m=0}^{M/2-1} \sum_{n=0}^N \tilde{v}(m, n, t) \exp(ik_m x) T_n(y) \quad (14)$$

where M and $N + 1$ are the number of grid points in the x and y directions, respectively, $k_m = 2\pi m/L_x$ is the m th wavenumber in the x direction, and $L_x = 5$ (see Fig. 1) is the length of the computation domain in the x direction. The grid points x_m and y_n are spaced as follows

$$x_m = \frac{mL_x}{M}, \quad m = 0, 1, \dots, M-1 \quad (15a)$$

$$y_n = \cos(\pi n/N), \quad n = 0, 1, \dots, N \quad (15b)$$

The Chebyshev polynomials are related to the cosine functions by

$$T_n(y) = \cos(n\theta), \quad \theta = \cos^{-1}y \quad (16)$$

By rewriting the double sum given in Eq. (14) as the following single sum

$$v(x, y, t) = \sum_{m=0}^{M/2-1} \tilde{v}(m, y, t) \exp(ik_m x) \quad (17)$$

we reduce the problem over the $M \times (N + 1)$ physical points to the consideration of the $M/2$ transform variables at each time step. In terms of the transform variables, Eq. (11a), which is the only equation which must be advanced in time, takes the form

$$\frac{\partial^2 \tilde{\zeta}_{pm}^{n+1}}{\partial y^2} - \left[k_m^2 + \frac{2Re}{\Delta t} \right] \tilde{\zeta}_{pm}^{n+1} = G(y, k_m, \tilde{\zeta}_m^n, \tilde{F}_m^n, \tilde{F}_m^{n-1}) \quad (18)$$

In the above, use has been made of the fact that the operation $\partial/\partial x$ in physical space corresponds to multiplication by ik_m in transform space. Due to the presence of the nonlinear terms \tilde{F}_m^n and \tilde{F}_m^{n-1} it is necessary, at each time step, to inverse transform to physical space, perform the operations required to obtain F , and then transform F to get \tilde{F} . We perform these transforms by using standard Fast Fourier Transform techniques. Also, to avoid aliasing errors, whereby energy from modes outside our range of consideration is placed into lower modes, we use the well known de-aliasing technique whereby we consider $3M/2$ physical points but use only the modes corresponding to M points.

We remark that the transform variable $\tilde{\zeta}_{pm}^{n+1}$ itself contains a series of $N + 1$ Chebyshev polynomials (compare Eqs. (14) and (17)). However, by using recursion relations which relate derivatives of a Chebyshev function of order n to neighboring orders, the second derivative in Eq. (18) for the $N + 1$ grid points gives rise to two quasi-tridiagonal matrices for the coefficients of the even and odd Chebyshev polynomials [13]. Inversion of these matrices is considerably less time consuming than full matrices of the same order.

Boundary Conditions

At the lower boundary $y = -1$ we use the shear-free condition $\partial u/\partial y = 0$ to minimize its effect on the interaction of the vortices with the upper boundary, our principal interest. At the upper boundary

$y = 1$ we consider three conditions. Two are the standard fixed shear-free and no-slip ($u = 0$) conditions, as considered in [5]. The third is the novel condition of the presence of a surface contaminant which is adsorbed on the water surface, or surfactant. In this case the surface tension on the water surface γ varies a function of the surfactant concentration σ . In the case where σ varies with x on the surface, Fig. 2 shows that a shear stress occurs, given by

$$\frac{\partial u}{\partial y} = Re \frac{\partial \gamma(\sigma)}{\partial x} \quad (19)$$

In terms of our formulation, which considers the velocity v in transform space, the above condition takes the form

$$\frac{\partial^2 \bar{v}}{\partial y^2} = Re k_m^2 \bar{\gamma}, \text{ for } m = 0, 1, 2, \dots, M/2 - 1 \quad (20)$$

Eqs. (19) and (20) indicate that it is necessary to solve the following transport equation for the concentration σ in order to determine the shear stress condition at the surface

$$\frac{\partial \sigma}{\partial t} = \frac{1}{Rs} \frac{\partial^2 \sigma}{\partial x^2} - \frac{\partial(u\sigma)}{\partial x} \quad (21)$$

where $Rs = V_0 a / \beta$ is the Reynolds number for the surfactant, and β is the surfactant diffusion coefficient. We solve Eq. (21) implicitly for the concentration σ but couple it explicitly with the surface velocity u . By using the previously mentioned Crank-Nicholson method for the linear diffusion term and the Adams-Bashforth method for the nonlinear convection term, Eq. (21) takes the following form in transform space

$$\begin{aligned} & \bar{\sigma}_m^{n+1} \left(1 + \frac{k_m^2 \Delta t}{2Rs} \right) \\ &= \bar{\sigma}_m^n \left(1 - \frac{k_m^2 \Delta t}{2Rs} \right) + \frac{ik_m \Delta t}{2} (-3u \bar{\sigma}_m^n + u \bar{\sigma}_m^{n-1}) \end{aligned} \quad (22)$$

It is well known that it is, in general, necessary to solve the boundary condition Eq. (21) or (22) iteratively with the previous formulation for the main flow until the concentration σ calculated for two successively updated values of u agree to within a given error tolerance ϵ . The boundary condition would, in fact, require repeated calculations of the main flow, with sharply increased computer cost.

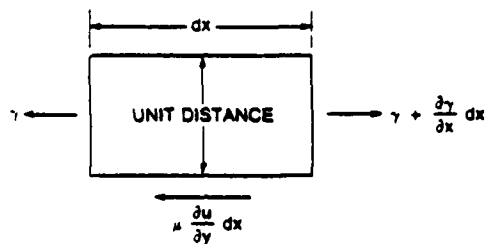


Fig. 2 — Shear Stress Due to Nonuniform Surfactant Concentration

We have adopted a series of approximations which render the calculation time to be nearly the same as for the fixed shear-free and no-slip conditions. First, in order to avoid a mismatch between the time step requirements for the boundary condition and main flows, we take $Rs = Re$. We note that numerical values for the diffusion coefficient of surfactants are not well known and that for the relatively high Re used in our study ($Re = 5000$), the value of Rs has only a secondary effect

in Eq. (22). Secondly, we consider only slow and moderate variations of γ with σ . The experimental data surveyed by Skop, Brown, and Lindsley [14] show that the variation of γ with σ may be approximated by several line segments, with slopes $|A'|$ which are typically less than 30 ergs/ μg or more than 300 ergs/ μg . We use the absolute value sign since A' is a negative number; i.e., γ decreases with increasing σ . We find that that we must restrict $|A'|$ to be less than approximately 60 ergs/ μg to prevent significant numerical instability. We have been able to extend the range of A' by using numerical damping techniques such as increasing the value of Rs or adding a higher order diffusion term involving $\partial^4/\partial x^4$ in Eq.(21), or (which is most convenient in our spectral approach) directly filtering out the higher modes in Eq. (22). We have not extensively pursued these techniques since we feel that excessively high damping will be needed to stabilize the calculations of the shock-like behavior at the high end of $|A'|$. Also, as shown later, our results at the upper end of the numerically stable $|A'|$ range already resemble those for the no-slip case.

Initial Conditions

The initial position of our vortices is as shown in Fig. 1. For the Gaussian vortices considered in our study, the vorticity ω_i , $i = 1, 2$, of each vortex is given by

$$\omega_i(x, y) = \frac{\Gamma_i}{\pi r^2} \exp -[(x - x_i)^2 + (y - y_i)^2]/r^2 \quad (23)$$

where $x_1 = -0.5$, $x_2 = +0.5$, $y_1 = y_2 = -0.75$, and $r = 0.25$ is a measure of the core size. The unit distance between the vortices and a value of $\Gamma_i = 2\pi$ give an initial unit vortex velocity, in accordance with our nondimensionalization approach, discussed in connection with Eq. (1). The total vorticity ω is given by

$$\omega = \frac{\partial v}{\partial x} - \frac{\partial u}{\partial y} = \sum_{i=1}^2 \omega_i \quad (24)$$

By taking first derivatives of the above equation with respect to x and y , and making use of the continuity Eq.(2), we obtain two second-order Poisson equations for the velocities u and v

$$\nabla^2 u = - \frac{\partial \omega}{\partial y} \quad (25a)$$

$$\nabla^2 v = + \frac{\partial \omega}{\partial x} \quad (25b)$$

Similar to what we have described for the time stepping procedure, we solve these equations in Fourier-Chebyshev transform space for the following boundary conditions. At the lower boundary $y = -1$, $v = \partial u / \partial y = 0$. At the upper boundary $y = +1$, $v = u = 0$ for the no-slip case, and $v = \partial u / \partial y = 0$ for the shear-free and surface contaminant cases. We note here that the latter two cases have identical initial conditions since we take the initial surfactant distribution $\sigma(x)$ to be uniform.

NUMERICAL RESULTS

Calculation Parameters

We perform our calculations over a 32×33 grid in the x and y directions, respectively, which corresponds to $M = N = 32$. The value of Re is taken to be 5000. The dimensions of our computation domain, in terms of the initial vortex spacing, is 2 units in the y direction, and 5 units in the x direction. These are equal to those used in [8]. In the following, we first present contour plots of u , v , and ω for the main flow and then line plots of u , v , and ω at the surface for various times t . We note that $t = 1$ corresponds to the time required to

travel a unit distance at the initial vortex velocity. The results are presented for the no-slip, shear-free, and various surfactant cases. The contour plots are shown for $A' = -5.4$ ergs/ μg , while the line plots are shown for four values of A' : -1.8 , -5.4 , -18 , -54 ergs/ μg .

Contour Plots of Main Flow

Figures 3a, b, c respectively show plots of the velocity v for the shear-free case at $t = 0.5$, 1.5, 2.5. The results are very similar for the no-slip and surfactant cases with the exception that the calculations for the no-slip case had to be stopped for $t \geq 2$ due to numerical instability. It seems that for the high shear gradients in this case, a finer grid is necessary. These figures show the expected result that at $t = 0.5$, the vortices are near the lower boundary, rise to an intermediate position at $t = 1.5$, and flatten against the upper boundary at $t = 2.5$.

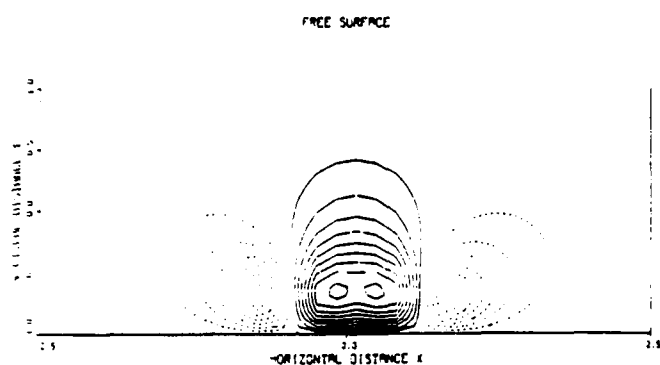


Fig. 3a — Velocity v for Shear-Free Case at $t = 0.5$

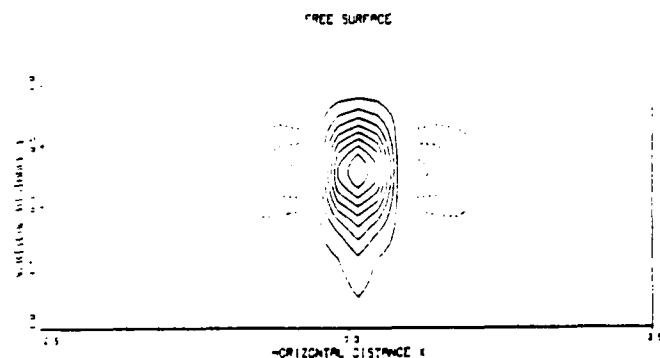


Fig. 3b — Velocity v for Shear-Free Case at $t = 1.5$

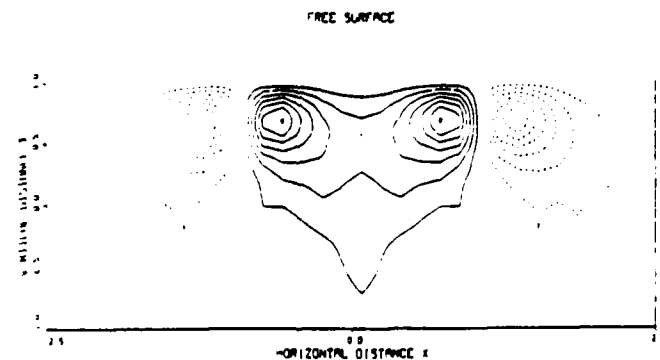


Fig. 3c — Velocity v for Shear-Free Case at $t = 2.5$

The differences due to the various surface conditions are larger in the case of u , and are largest in the case of ω . Figures 4a, b, c respectively show plots of u for the shear-free, surfactant, and no-slip conditions at $t = 1.5$, while Figs. 5a, b show plots of u for the first two cases at $t = 2.0$. Figures 6a, b, c and Figs. 7a, b show corresponding results for the vorticity ω at $t = 1.5$ and 2.5. Figures 4 and 6 show the expected result that the surfactant case lies intermediate between the shear-free and no-slip conditions. In particular, the surfactant case tends to exhibit the main flow shape of the shear-free case and (to some extent) the surface shear characteristics of the no-slip case. Figures 5 and 7 show that the differences between the shear-free and surfactant cases are greater at the later times. Now even the main flow shapes of the two cases are perceptibly different, particularly in the case of ω .

We also note that the relative lack of gradients in the shear-free flow case leads to the computation being stable over a longer time than the other two cases.

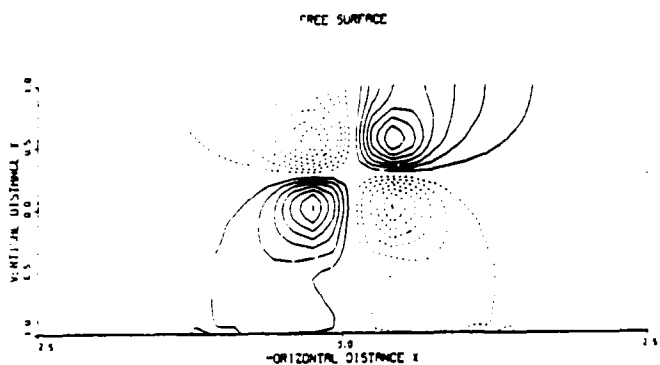


Fig. 4a — Velocity u for Shear-Free Case at $t = 1.5$

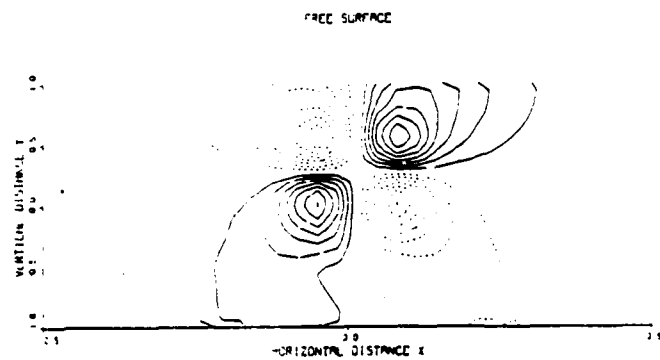


Fig. 4b — Velocity u for Surfactant Case at $t = 1.5$

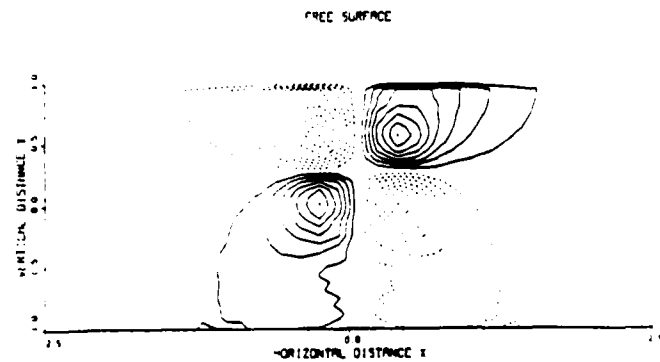


Fig. 4c — Velocity u for No-Slip Case at $t = 1.5$

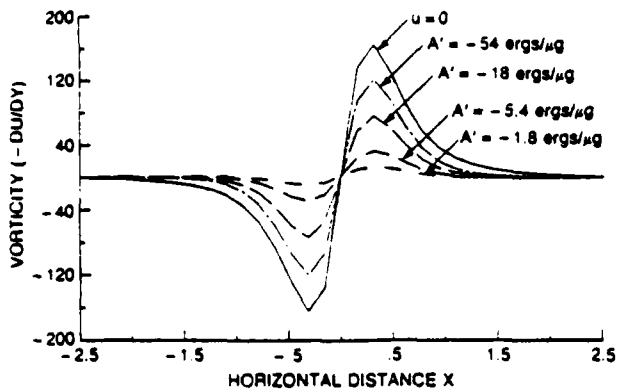


Fig. 8a — Surface Vorticity ω at $t = 1$

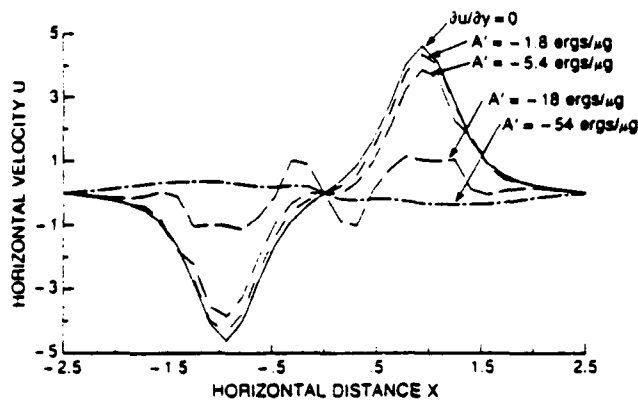


Fig. 8b — Surface Velocity u at $t = 2$

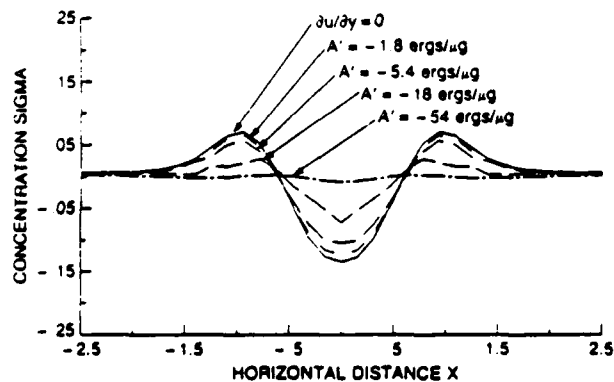


Fig. 8c — Surface Surfactant Concentration $\Delta\sigma$ at $t = 2$

CONCLUSIONS

We have presented a spectral method involving transforms in Fourier-Chebyshev space to solve the two-dimensional incompressible Navier-Stokes equations describing the evolution of the flow due to a pair of vortices rising to a surface. The use of these transform methods converts, at each time step, the calculation over the physical grid to a series of Poisson equations for the Fourier modes. The solution of each Fourier mode amounts to the solution of sets of sparse algebraic equations for the coefficients of the Chebyshev modes. By combining the continuity equation with derivatives of the momentum equations, we arrive at a fourth-order formulation which eliminates the troublesome pressure term.

At the surface towards which the vortices are rising, we consider three boundary conditions: the traditional fixed no-slip and shear-free conditions, and a novel condition of variable shear due to the presence of an adsorbing surface contaminant (or surfactant), which changes the surface tension at the fluid surface. Our solution of the additional transport equation modeling the surfactant concentration is stable, without using iterative or numerical damping techniques, for low and moderate magnitudes of the surfactant surface tension-concentration slopes. Contour plots of the main flow below the surface show the expected trend that the surfactant case lies intermediate between the no-slip and shear-free cases. The differences are quite small for the vertical velocity v , moderate for the horizontal velocity u , and large for the vorticity ω . Line plots of u , ω , and $\Delta\sigma$ (the deviation of the concentration from the initial uniform distribution) for the surface flow show the manner in which the behavior of the surfactant cases changes from that of the shear-free case to resemble the no-slip case with increasing magnitudes of the surface tension-concentration slope.

REFERENCES

- Leonard, A., "Vortex Methods for Flow Simulation," *Journal of Computational Physics*, Vol. 37, 1980, pp. 289-335.
- Saffman, P.G. and Baker, G.R., "Vortex Interactions," *Annual Review of Fluid Mechanics*, Vol. 11, 1979, pp. 95-122.
- Sarpkaya, T., "Computational Methods with Vortices—The 1988 Freeman Scholar Lecture," *Journal of Fluids Engineering*, Vol. 111, 1989, pp. 5-52.
- Ersay, S. and Walker, J.D.A., "Viscous Flow Induced by Counter-Rotating Vortices," *Physics of Fluids*, Vol. 28, No. 9, 1985, pp. 2687-2698.
- Peace, A.J. and Riley, N., "A Viscous Vortex Pair in Ground Effect," *Journal of Fluid Mechanics*, Vol. 129, 1983, pp. 409-426.
- Sarpkaya, T., "Trailing-Vortex Wakes on the Free Surface," 16th Symposium on Naval Hydrodynamics, 1986, pp. 38-50.
- Willmarth W.W., Tryggvason, G., Hirs, A., and Yu, D., "Vortex Pair Generation and Interaction with a Free Surface," *Physics of Fluids*, Vol. A1, No. 2, 1989, pp. 170-172.
- Yu, D. and Tryggvason, G., "The Free Surface Signature of Unsteady, Two-Dimensional Vortex Flows," University of Michigan Program in Ship Hydrodynamics Report 89-03, 1989.
- Ohring, S. and Lugt, H.J., "Two Counter-Rotating Vortices Approaching a Free Surface in a Viscous Fluid," David Taylor Research Center Report DTRC-89/013, 1989.
- Hussaini, M.Y. and Zang, T.A., "Spectral Methods in Fluid Dynamics," *Annual Review of Fluid Mechanics*, Vol. 19, 1987, pp. 339-367.
- Handler, R.A., Hendricks, E.W., and Leighton, R.I., "Low Reynolds Number Calculation of Turbulent Channel Flow: A General Discussion," Naval Research Laboratory Memorandum Report 6410, 1989.
- Kim, J., Moin, P., and Moser, R., "Turbulence Statistics in Fully Developed Channel Flow at Low Reynolds Number," *Journal of Fluid Mechanics*, Vol. 177, 1987, pp. 133-166.
- Canuto, C., Hussaini, M.Y., Quarteroni, A., and Zang, T.A., *Spectral Methods in Fluid Dynamics*, Springer-Verlag, New York, NY, 1987.
- Skop, R.A., Brown, J.W., and Lindsley, W.G., "Bubble Transport of Surface-Active Organic Compounds in Seawater: Initial Measurements and Results," University of Miami Report RSMAS-TR89-003, 1989.

APPENDIX B

A Finite Element Solver for Axisymmetric Compressible Flows

A FINITE ELEMENT SOLVER FOR AXISYMMETRIC COMPRESSIBLE FLOWS

Rainald Löhner^{*}, Joseph D. Baum[†], Eric Loth[†] and Ravi Ramamurti[‡]

^{*} CMEE, The George Washington University, Washington, D.C.

[†] LCP&FD, Naval Research Laboratory, Washington, D.C.

[‡] Science Applications International Corp., MacLean, VA

Abstract

This paper describes an extension of previously developed methodologies for solving the Euler and Navier-Stokes equations with unstructured grids in cartesian coordinate systems [1-5] to axisymmetric coordinate systems. It is shown how to arrive at a consistent, high-order formulation by proper choice of interpolation for the unknowns. An exact integration of all integrals is performed, and the exact formulae are derived and presented. Numerical examples simulating both transient and steady-state flows in the subsonic, transonic and supersonic regime are given. They demonstrate the accuracy and wide range of applicability of the method.

Introduction

Axisymmetric compressible flow problems need to be simulated in many practical situations, including flows in or past bodies of revolution at zero angle of attack, such as pipes, nacelles, fuselages, missiles, as well as certain types of explosions and detonations. For an axisymmetric coordinate system, the Navier-Stokes equations governing compressible flows may be written as:

$$\frac{\partial U}{\partial t} + \frac{\partial F_a^z}{\partial z} + \frac{1}{r} \frac{\partial F_a^r}{\partial r} = \frac{S_a}{r} + \frac{\partial F_v^z}{\partial z} + \frac{1}{r} \frac{\partial F_v^r}{\partial r} + \frac{S_v}{r}, \quad (1a)$$

where

$$U = \begin{Bmatrix} \rho \\ \rho u \\ \rho v \\ \rho e \end{Bmatrix}, F_a^z = \begin{Bmatrix} \rho u \\ \rho u^2 + p \\ \rho uv \\ uH \end{Bmatrix}, F_a^r = \begin{Bmatrix} r\rho v \\ r\rho uv \\ r\rho v^2 + rp \\ rvH \end{Bmatrix}, \quad (1b-d)$$

$$H = \rho e + p, S_a = \begin{Bmatrix} 0 \\ 0 \\ p \\ 0 \end{Bmatrix}, \quad (1e-f)$$

$$F_v^z = \begin{Bmatrix} 0 \\ \tau^{zz} \\ \tau^{rz} \\ u\tau^{zz} + v\tau^{rz} + q_z \end{Bmatrix}, S_v = \frac{1}{Re} \begin{Bmatrix} 0 \\ 0 \\ \tau^{\theta\theta} \\ 0 \end{Bmatrix}, \quad (1g-h)$$

$$F_v^r = \begin{Bmatrix} 0 \\ r\tau^{rz} \\ r\tau^{rr} \\ u\tau^{rz} + v\tau^{rr} + r q_r \end{Bmatrix}, \quad (1i)$$

Here z, r denote the axial and radial coordinates. ρ, p, e, H denote the density, pressure, energy and enthalpy, u, v denote the velocities in the z and r direction. Using Stokes hypothesis, the viscosity coefficient μ and the bulk modulus λ are related by

$$\lambda = -\frac{2\mu}{3}, \quad (2)$$

and the viscous shear stresses and heat fluxes are given by

$$\tau^{zz} = 2\mu \frac{\partial u}{\partial z}, \tau^{rr} = 2\mu \frac{\partial v}{\partial r}, \quad (3a, b)$$

$$\tau^{\theta\theta} = -2\mu \frac{v}{r}, \tau^{rz} = \mu \left(\frac{\partial u}{\partial r} + \frac{\partial v}{\partial z} \right), \quad (3c, d)$$

$$q^z = k \frac{\partial T}{\partial z}, q^r = k \frac{\partial T}{\partial r}, \quad (3e, f)$$

where T and k denote the temperature and thermal conductivity of the fluid respectively. The equation set is completed by the addition of the state equations

$$p = (\gamma - 1)\rho \left[e - \frac{1}{2}(u^2 + v^2) \right], \quad (4a, b)$$

$$T = c_v \left[e - \frac{1}{2}(u^2 + v^2) \right],$$

which are valid for a perfect gas, where γ is the ratio of the specific heats and c_v is the specific heat at constant volume.

Multiplication of the system of Eqs. (1) with r yields

$$\frac{\partial rU}{\partial t} + \frac{\partial rF_a^z}{\partial z} + \frac{\partial F_a^r}{\partial r} = S_a + \frac{\partial rF_v^z}{\partial z} + \frac{\partial F_v^r}{\partial r} + S_v, \quad (5)$$

We will denote the form of the Euler equations as given by Eq.(1) as form 1, and the form given by Eq.(3) as Form 2. Both forms have been used as

starting points for discrete approximations. Form 1 was used by Kutler, Chakravarthy and Lombard [6], who treated it as a system of equations in two dimensions. This straightforward use of form 1 does not produce a conservative difference scheme, and therefore these authors employed a shock fitting scheme to trace the shocks. Form 2 was employed by Deese and Agarwal [7], Yu and Chen [8], and Woan [9]. These authors used this form in Jameson's two-dimensional cell-centered finite volume FLO52 code. Because the scheme is cell-centered, no problems appear at $r = 0$ (no nodes are placed there). However, problems are expected at $r = 0$ if a node-centered scheme is preferred.

Two-Step Taylor-Galerkin

The two-step Taylor-Galerkin algorithm has been used extensively for the computation of both inviscid and viscous flows in two and three dimensions for Cartesian coordinate systems [3-5]. Given a system of partial differential equations of the form:

$$\frac{\partial U}{\partial t} + \frac{\partial F_a^i}{\partial x^i} = S_a + \frac{\partial F_v^i}{\partial x^i} + S_v, \quad (6)$$

where U, F^i and S denote the vectors of unknowns, fluxes and source terms, we proceed as follows:

a) First step: (Advective Predictor)

$$U^{n+\frac{1}{2}} = U^n + \frac{\Delta t}{2} \cdot \left(S_a |^n - \frac{\partial F_a^i}{\partial x^i} |^n \right) \quad (7)$$

b) Second step:

$$\Delta U^n = U^{n+1} - U^n = \Delta t \cdot \left(S_a |^{n+\frac{1}{2}} - \frac{\partial F_a^i}{\partial x^i} |^{n+\frac{1}{2}} + S_v |^n + \frac{\partial F_v^i}{\partial x^i} |^n \right). \quad (8)$$

In both substeps the spatial discretization is performed via the usual Galerkin weighted residual method [3-5]. However, we note that at $t^{n+\frac{1}{2}} = t^n + \frac{1}{2}\Delta t$, the quantities U, F, S are assumed as piecewise constant in the elements, whereas at t^n, t^{n+1} , the quantities U, F, S are assumed piecewise linear.

Choice of Conservative Form and Interpolation

Having selected the time-marching algorithm, we are now faced with the choice of conservative form. We can either:

a) Take Conservative form 1, and integrate consistently, e.g.,

$$\int_{\Omega} W \frac{\partial U}{\partial t} 2 \pi r dz dr, \quad (9)$$

which yields essentially conservative form 2. or

b) Take Conservative form 2, interpret it as a two-dimensional cartesian problem, and incorporate it 'as is' into an existing 2-D code.

It is interesting to note that whichever approach we take, we always require conservative form 2 in order to obtain a consistent, conservative scheme. The next question that arises is how to interpolate the unknowns involved in order to obtain a discretization scheme. We can:

a) Interpolate ($r\rho, r\rho u, r\rho v, r\rho e$) by a piecewise linear approximation. This is the so-called 'group formulation'. It appears very economical and simple to implement, but for the limit as $r \rightarrow 0$, all derived quantities, such as the pressure, are not defined. They have to be obtained either using L'Hopital's rule (which involves taking derivatives), or the points lying on the axis $r = 0$ have to be pushed to $r = \epsilon$, where ϵ is a small number. We tried this option, but found that we always encountered numerical problems close to the axis $r = 0$.

b) Interpolate ($\rho, \rho u, \rho v, \rho e$) and r by a piecewise linear approximation. This form yields a higher accuracy in the r -direction [10] and has no problems at $r = 0$. The integrals that appear in the weighted residual statement are more complicated to evaluate. However, they may still be derived in closed form. For these reasons we chose this second form for the spatial discretization of the Euler equations.

The First Step

Evaluating all the integrals in the weighted residual statement of Eq.(5) and using the notation defined in Figure 1, and the expressions

$$r'_i = \frac{r_i}{\bar{r}_{el}}; \quad \bar{r}_{el} = \frac{r_A + r_B + r_C}{3}, \quad (10)$$

the following discretization for the Navier-Stokes equations results:

Continuity:

$$\begin{aligned} \bar{r}_{el} &= \frac{1}{12} \sum_{j=1,3} (3 + r'_j) \rho_j \\ &- \frac{\Delta t}{2} \sum_{j=1,3} [N_x^j(\rho u)_j + N_r^j(\rho v)_j] \\ &- \frac{\Delta t}{2} \frac{1}{\bar{r}_{el}} \frac{1}{3} \sum_{j=1,3} (\rho v)_j \end{aligned} \quad (11)$$

X-Momentum:

$$\begin{aligned} \bar{\rho u}_{el} &= \frac{1}{12} \sum_{j=1,3} (3 + r'_j)(\rho u)_j \\ &- \frac{\Delta t}{2} \sum_{j=1,3} [N_{,s}^j(\rho u^2 + p)_j + N_{,r}^j(\rho uv)_j] \quad (12) \\ &- \frac{\Delta t}{2} \frac{1}{\bar{r}_{el}} \frac{1}{3} \sum_{j=1,3} (\rho uv)_j \end{aligned}$$

R-Momentum:

$$\begin{aligned} \bar{\rho v}_{el} &= \frac{1}{12} \sum_{j=1,3} (3 + r'_j)(\rho v)_j \\ &- \frac{\Delta t}{2} \sum_{j=1,3} [N_{,s}^j(\rho uv)_j + N_{,r}^j(\rho v^2 + p)_j] \quad (13) \\ &- \frac{\Delta t}{2} \frac{1}{\bar{r}_{el}} \frac{1}{3} \sum_{j=1,3} (\rho v^2)_j \end{aligned}$$

Energy:

$$\begin{aligned} \bar{\rho e}_{el} &= \frac{1}{12} \sum_{j=1,3} (3 + r'_j)(\rho e)_j \\ &- \frac{\Delta t}{2} \sum_{j=1,3} [N_{,s}^j(uH)_j + N_{,r}^j(vH)_j] \quad (14) \\ &- \frac{\Delta t}{2} \frac{1}{\bar{r}_{el}} \frac{1}{3} \sum_{j=1,3} (vH)_j \end{aligned}$$

The Second Step

For the second step, we again evaluate all the integrals exactly. Denoting $N_{,j}^i$ as the derivative of the shape function N^i with respect to j , and M_e as the consistent mass matrix

$$M_e = \int N^i N^j r dz dr, \quad (15)$$

we obtain for the Euler equations:

Continuity:

$$M_e \Delta \rho = \Delta t \sum_{el} VOL_{el} \bar{r}_{el} \left[N_{,s}^i \bar{\rho u}_{el} + N_{,r}^i \bar{\rho v}_{el} \right] \quad (16)$$

X-Momentum:

$$\begin{aligned} M_e \Delta \rho u &= \Delta t \sum_{el} VOL_{el} \bar{r}_{el} \left[N_{,s}^i ((\overline{\rho u^2 + p})_{el} - \tau_{el}^{xx}) \right. \\ &\quad \left. + N_{,r}^i (\overline{\rho uv}_{el} - \tau_{el}^{xz}) \right] \quad (17) \end{aligned}$$

R-Momentum:

$$\begin{aligned} M_e \Delta \rho v &= \Delta t \sum_{el} VOL_{el} \bar{r}_{el} \left[N_{,s}^i (\overline{\rho uv}_{el} - \tau_{el}^{xz}) \right. \\ &\quad \left. + N_{,r}^i ((\overline{\rho v^2 + p})_{el} - \tau_{el}^{rr}) \right] \\ &+ \Delta t \sum_{el} VOL_{el} N^i (\bar{p}_{el} + \tau_{el}^{\theta\theta}) \quad (18) \end{aligned}$$

Energy:

$$\begin{aligned} M_e \Delta \rho e &= \\ \Delta t \sum_{el} VOL_{el} \bar{r}_{el} &\left[N_{,s}^i (\overline{uH}_{el} - (u\tau^{xx} + v\tau^{xz} + q_x)_{el}) \right. \\ &\quad \left. + N_{,r}^i (\overline{vH}_{el} - (u\tau^{xz} + v\tau^{rr} + q_r)_{el}) \right] \quad (19) \end{aligned}$$

Consistent Mass Matrices

A question that arises from the computational point of view is whether the consistent mass matrix, which is obtained by assembling, at element level, the following exact element matrices

$$\begin{aligned} M_e &= \frac{VOL_{el}}{60} \left[r_A \begin{pmatrix} 6 & 2 & 2 \\ 2 & 2 & 1 \\ 2 & 1 & 2 \end{pmatrix} + r_B \begin{pmatrix} 2 & 2 & 1 \\ 2 & 6 & 2 \\ 1 & 2 & 2 \end{pmatrix} + \right. \\ &\quad \left. r_C \begin{pmatrix} 2 & 1 & 2 \\ 1 & 2 & 2 \\ 2 & 2 & 6 \end{pmatrix} \right], \quad (20) \end{aligned}$$

cannot be simplified by taking the average element radius in the integral (13). This would yield the element matrix

$$M_e = \frac{VOL_{el} \bar{r}_{el}}{12} \begin{pmatrix} 2 & 1 & 1 \\ 1 & 2 & 1 \\ 1 & 1 & 2 \end{pmatrix} = \bar{r}_{el} M_e^{2D}, \quad (21)$$

which is less expensive to evaluate. Our numerical experiments indicate that this simplification can be employed without loss of accuracy. The consistent mass

matrix is solved iteratively as in the cartesian case [1-5], and again it is found that two to three passes over the elements are sufficient to raise the phase accuracy of the resulting scheme from second to essentially fourth order.

Artificial Viscosities

a) Modified Lapidus artificial viscosity: The modified Lapidus artificial viscosity [11], which proved successful for Cartesian coordinate systems, can be extended to the axisymmetric case without any further modifications by multiplying the element contributions by their respective average element radius.

b) Mass diffusion for the FEM-FCT algorithm: The mass diffusion which is added to the high-order scheme to yield a monotonic low-order scheme as part of the FEM-FCT algorithm [5] can also be extended to the axisymmetric case by simply multiplying the element contributions by their respective average element radius.

Numerical examples

A number of numerical examples are given to illustrate the performance of the method when simulating transient and steady-state problems in the subsonic, transonic and supersonic flow regime. For all the steady-state problems, local timestepping was used to accelerate the convergence.

1) Supersonic flow past a sphere (steady state): the case under consideration corresponds to a free-stream Mach Number of $M_\infty = 3.0$. For this steady-state case, only the Lapidus artificial viscosity was employed to stabilize the solution. The exact stand-off distance for the shock should be of $s = 1.216R$, where R denotes the radius of the sphere [12]. The grid was adaptively remeshed three times [13]. The final solution is shown in Figures 2a-2c. The experimental stand-off distance is reproduced exactly by the solution.

2) Shock impinging on a blunt body (transient): The problem statement, as well as the solutions obtained at two different times are shown in Figures 3a-3f. A strong shock ($M_s = 10$), coming from the left, collides with the concave body displayed in Figure 3a. An adaptive refinement scheme for transient problems [14] was employed to resolve accurately all flow features. The mesh was adapted every 7 timesteps, and two levels of refinement were specified. The FEM-FCT option was invoked to maintain sharp shock-resolution. The main aim of this simulation was to demonstrate the good phase-accuracy and low numerical damping of the present scheme for this class of problems. As observed in earlier simulations of this class of problems [15-17] the concave shape of

the body affects the stability of the stand-off shock significantly. Figures 3g,h show the time-histories for the pressure at a two stations along the $r = 0$ -axis. Station 1 (Figure 3g) lies at the far right end of the domain, while station 7 lies shortly behind the final position of the shock. One can clearly observe a damped oscillation for the shock location. It takes many cycles for the shock to settle to its final position. This behaviour, which is not observed for convex bodies, was also seen in other numerical simulations and several wind-tunnel experiments [15-17].

3) Flow in an Underexpanded Nozzle (steady state): The problem statement, as well as adapted mesh and Mach number contours are shown in Figures 4a and 4b respectively. Several different runs were performed for this problem. Some had the FEM-FCT option switched on, others only employed the two-step scheme described above. They all showed the existence of the two shocks depicted in Figure 4b. The run reproduced here was done with a Lapidus artificial viscosity. Both shocks resulted from inadequate nozzle contouring, as shown in the contours of the Mach number in the region near the throat (Fig. 4c). The pressure ratio across the shock is significantly lower than the pressure decrease through the throat, though the gradients are higher. During convergence to steady state, the grid was adaptively remeshed three times. The maximum stretching ratio for the elements was set to $S = 6$. A comparison between the measured and predicted radial distribution of pressure at the exit plane is shown in Fig. 4d. Significant scatter is shown in the experimental data, while no data is available in the region of the multiple shock system. Nonetheless, the results demonstrate very good agreement over most of the exit plane. Some deviation is shown near the wall, no doubt due to wall boundary layer effects.

4) Flow past a sphere, $Re = 100$ (steady, viscous): Steady viscous flow past a sphere at a Mach-number of $Ma = 0.1$ and Reynolds-number of $Re = 100$ provides an important test example to evaluate the accuracy of the present scheme. No artificial viscosity was added for this subsonic case. The problem statement, as well as the results obtained, are shown in Figure 5. The grid employed for this case, shown in Fig. 5a, consists of a structured portion divided into triangles near the vicinity of the sphere and unstructured mesh elsewhere. From Fig. 5d, it can be seen that the recirculation zone extends upto 1.4D into the wake, measured from the center of the sphere. This compares well with experimental results [17]. Figure 5e shows the comparison of surface vorticity with earlier numerical results [18,19], and the agreement is good. The flow separates at an angle of approximately 123 deg.

Conclusions

We have described a Finite Element Solver for axisymmetric compressible flows. The Navier-Stokes equations are advanced forward in time using a two-step Taylor-Galerkin procedure. Due care was given to obtain a consistent integration of all variables. Although slightly more expensive than the equivalent 2-D scheme, the current formulation is the only one that yields full second order accuracy for all the unknowns in both the x and r-directions. A high-order, monotonicity preserving scheme is obtained by combining this basic two-step Taylor-Galerkin procedure with FEM-FCT techniques.

Future developments will center on extensions of the current explicit scheme to semi-implicit or implicit schemes.

Acknowledgements

This work was partially funded by the Defense Nuclear Agency and the Air Force Ballistic Missile Office through the Laboratory for Computational Physics and Fluid Dynamics of the Naval Research Laboratory.

References

- [1] J. Donea - A Taylor Galerkin Method for Convective Transport Problems; *Int. J. Num. Meth. Engng.* 20, 101-119 (1984).
- [2] R. Löhner, K. Morgan and O.C. Zienkiewicz - The Solution of Nonlinear Systems of Hyperbolic Equations by the Finite Element Method; *Int. J. Num. Meth. Fluids* 4, 1043-1063 (1984).
- [3] R. Löhner, K. Morgan, J. Peraire and O.C. Zienkiewicz - Finite Element Methods for High Speed Flows; AIAA-85-1531-CP (1985).
- [4] R. Löhner, K. Morgan and O.C. Zienkiewicz - An Adaptive Finite Element Procedure for High Speed Flows; *Comp. Meth. Appl. Mech. Eng.* 51, 441-465 (1985).
- [5] R. Löhner, K. Morgan, J. Peraire and M. Vahdati - Finite Element Flux-Corrected Transport (FEM-FCT) for the Euler and Navier-Stokes Equations; *Int. J. Num. Meth. Fluids* 7, 1093-1109 (1987).
- [6] P. Kutler, S.R. Chakravarthy and C.P. Lombard - Supersonic Flow Over Ablated Nozzles Using an Unsteady Numerical Procedure; AIAA Paper 78-213 (1978).
- [7] J.E. Deese and R.K. Agarwal - Calculation of Axisymmetric Inlet Flowfields Using the Euler Equations; AIAA Paper 83-1853 (1983).
- [8] N.J. Yu and H.C. Chen - Flow Simulations for Nacelle-Propeller Configurations Using Euler Equations; AIAA Paper 84-2143 (1984).
- [9] C.J. Woan - Euler Solution of Axisymmetric Flows About Bodies of Revolution Using a Multi-grid Method; AIAA Paper 85-0017 (1984).
- [10] P.L. Roe - Error Estimates for Cell-Vertex Solvers of the Compressible Euler Equations; ICASE Rep. 87-6 (1987).
- [11] R. Löhner, K. Morgan, and J. Peraire - A Simple Extension to Multidimensional Problems of the Artificial Viscosity due to Lapidus; *Comm. Appl. Num. Meth.* 1, 141-147 (1985).
- [12] J. Zierep - *Theoretische Gasdynamik*; G. Braun, Karlsruhe (1976).
- [13] R. Löhner - An Adaptive Finite Element Solver for Transient Problems with Moving Bodies; *Comp. Struct.* 30, 303-317 (1988).
- [14] R. Löhner - An Adaptive Finite Element Scheme for Transient Problems in CFD; *Comp. Meth. Appl. Mech. Eng.* 61, 323-338 (1987).
- [15] R. Bastianon - Unsteady Solution of the Flowfield over Concave Bodies - *ALAA J.* 7, 531-533 (1969).
- [16] I.O. Bohachevsky and R.N. Kostoff - Supersonic Flow over Convex and Concave Shapes with Radiation and Ablation Effects; *ALAA J.* 10, 1024-1031 (1972).
- [17] M. Van Dyke - *An Album of Fluid Motion*, Parabolic Press; (1982).
- [18] R. Clift, J.R. Grace and M.E. Weber - *Bubbles, Drops and Particles*, Academic Press, (1978).
- [19] Y. Rimon and S.I. Cheng - Numerical Solution of a Uniform Flow over a Sphere at Intermediate Reynolds Numbers; *Phys. Fluids* 12,5, (1969).

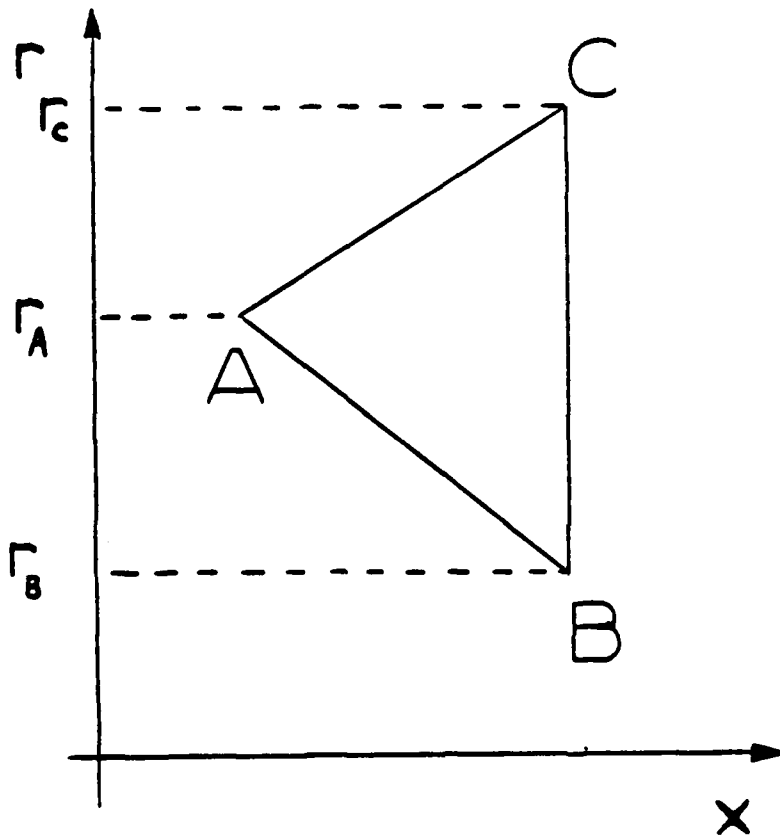


Figure 1: Notation used at element level

MIN= 0.00E+00 . MAX= 0.25E+01 .
OUC= 0.50E+00

MIN= 0.35E+00 . MAX= 0.12E+02 . MACH-NR
OUC= 0.35E+00

NELEM= 1348 . NP0IN= 729

IFSH

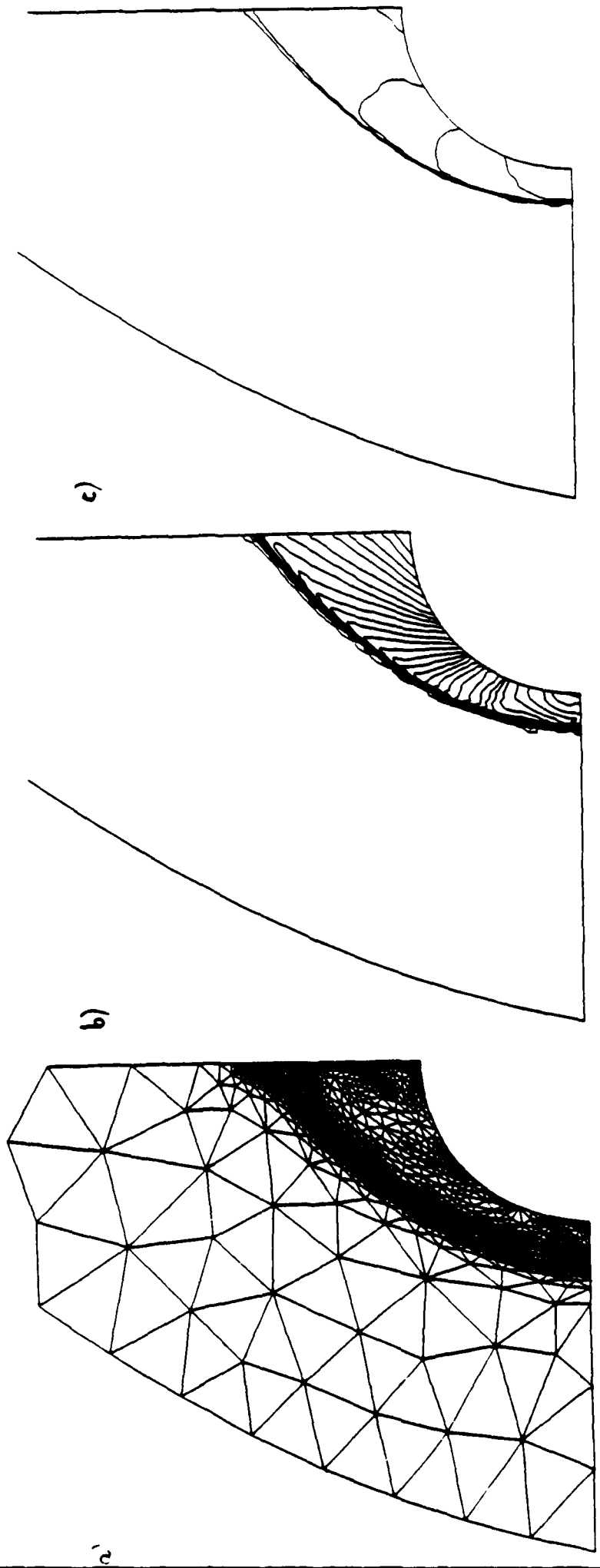


Figure 2 : Supersonic Flow Past a Sphere

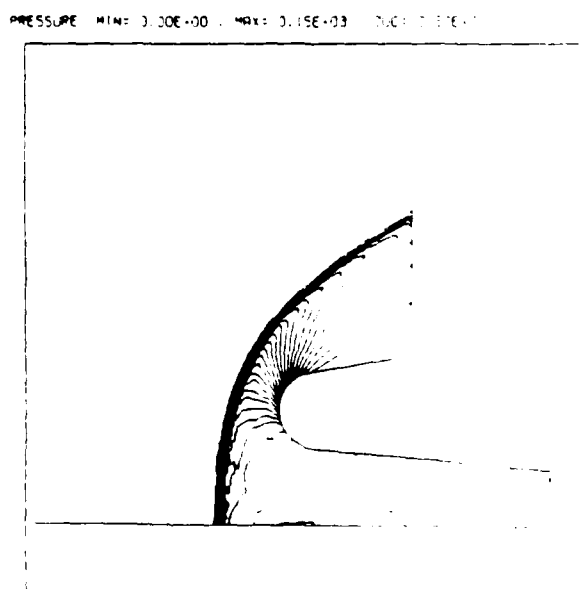
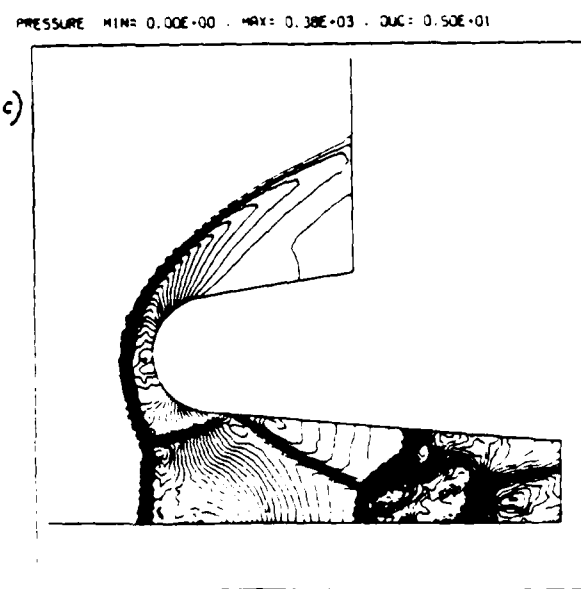
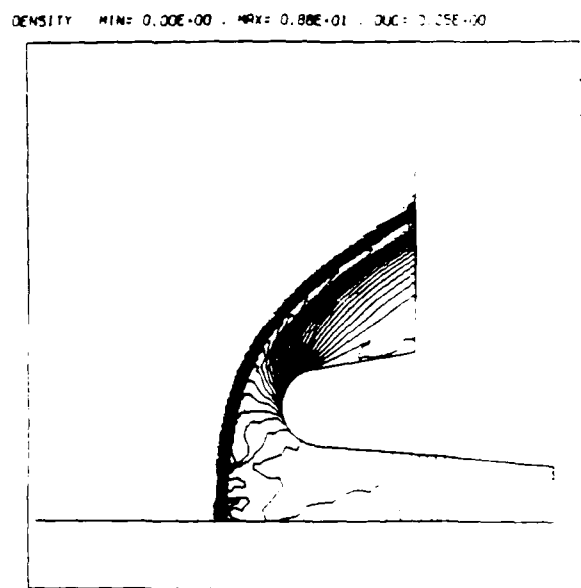
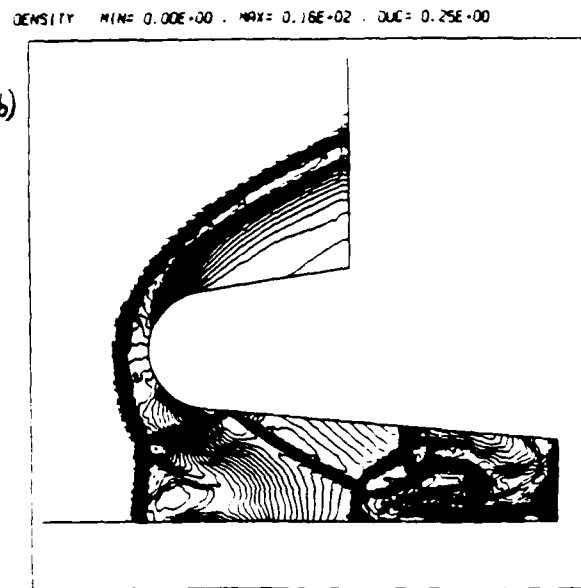
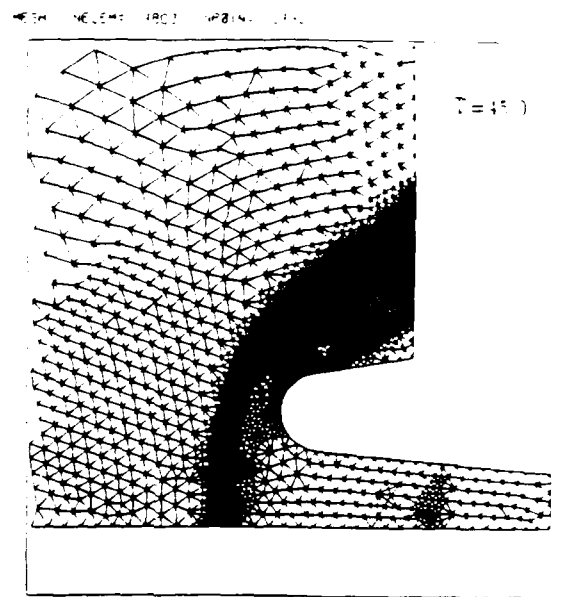
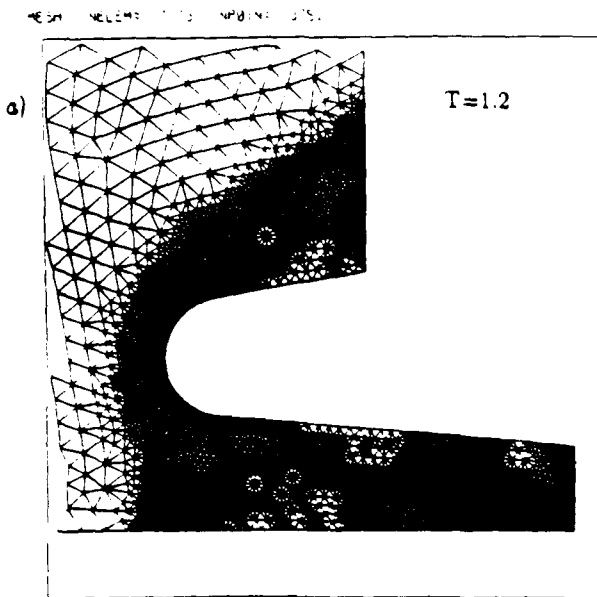


Figure 3 : Shock-Concave Body Interaction

Figure 3g: Shock-Concave Body Interaction: Pressure History at Station 1

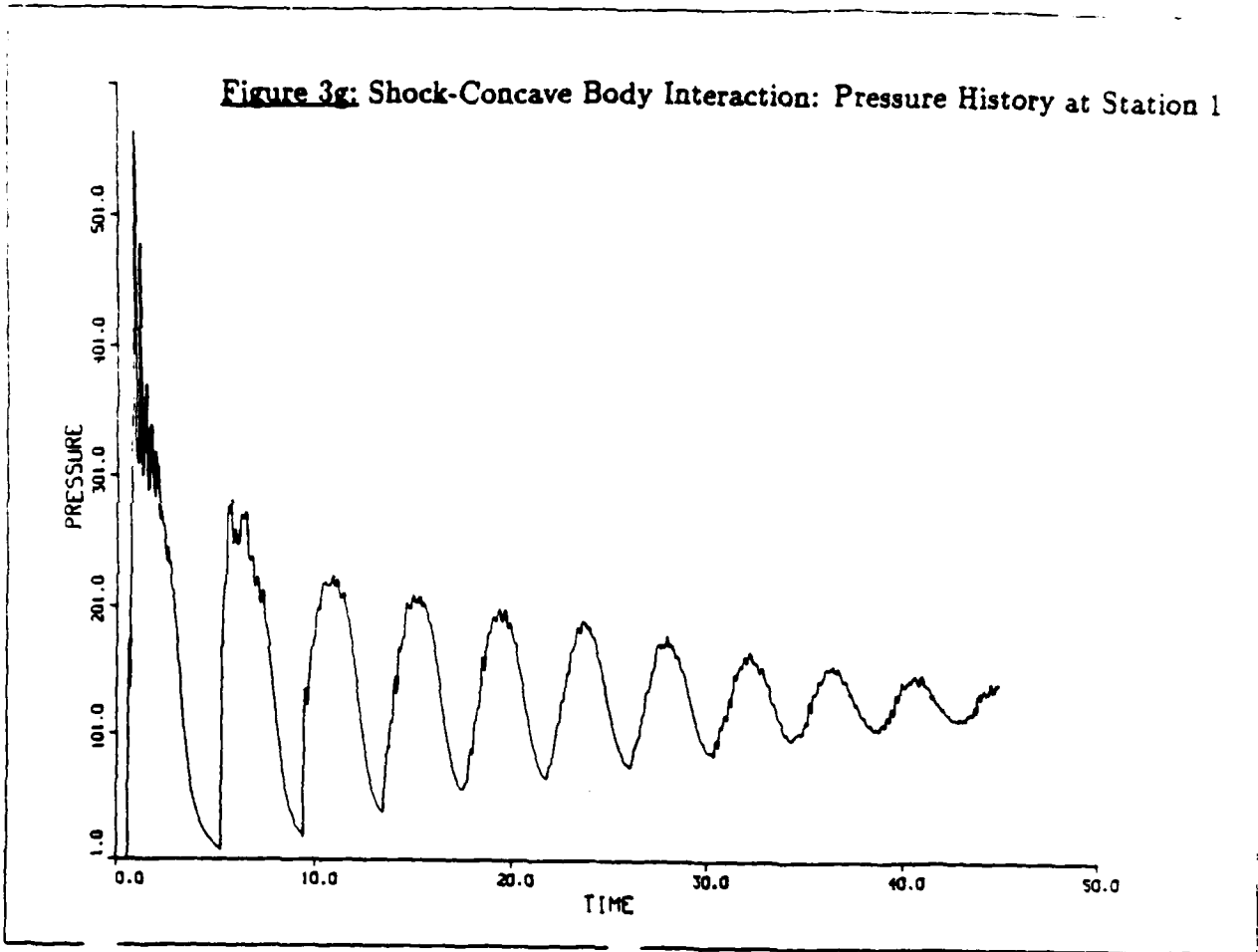
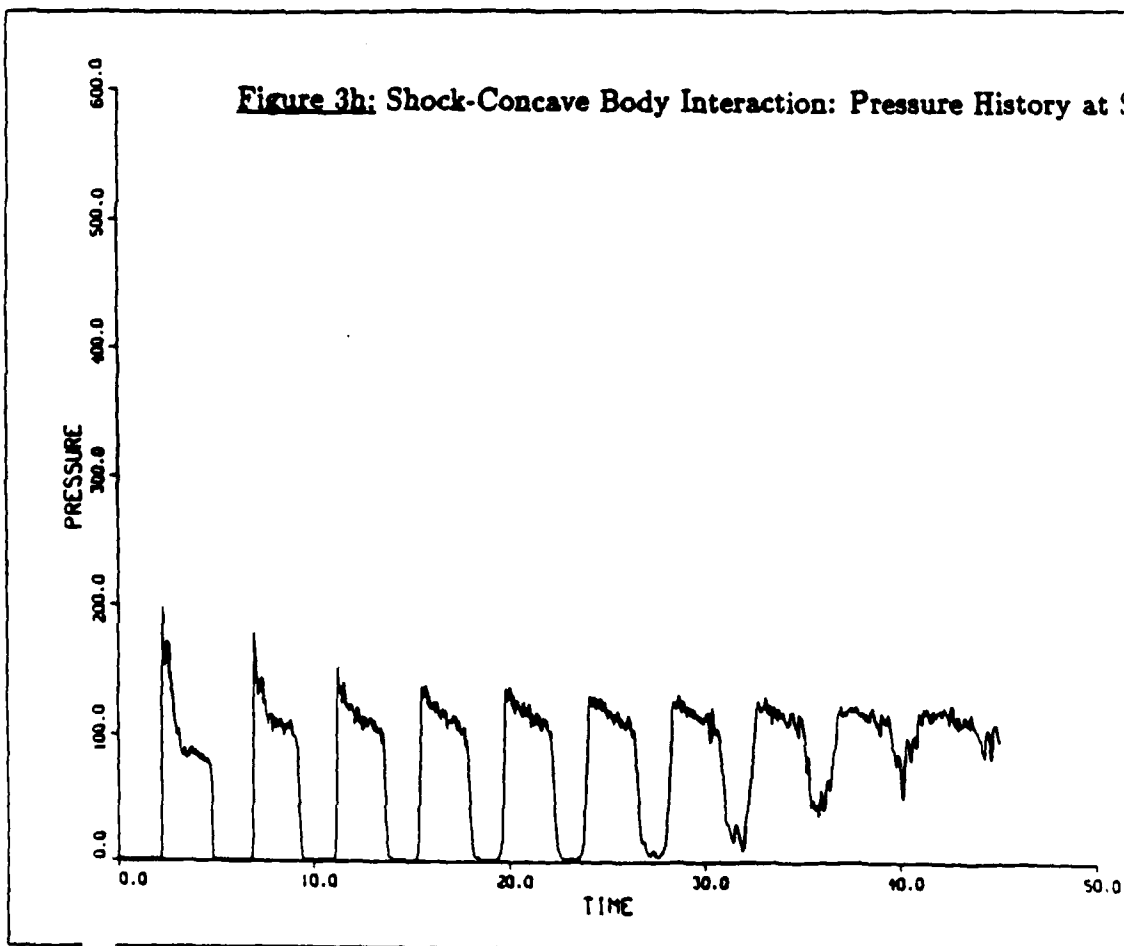
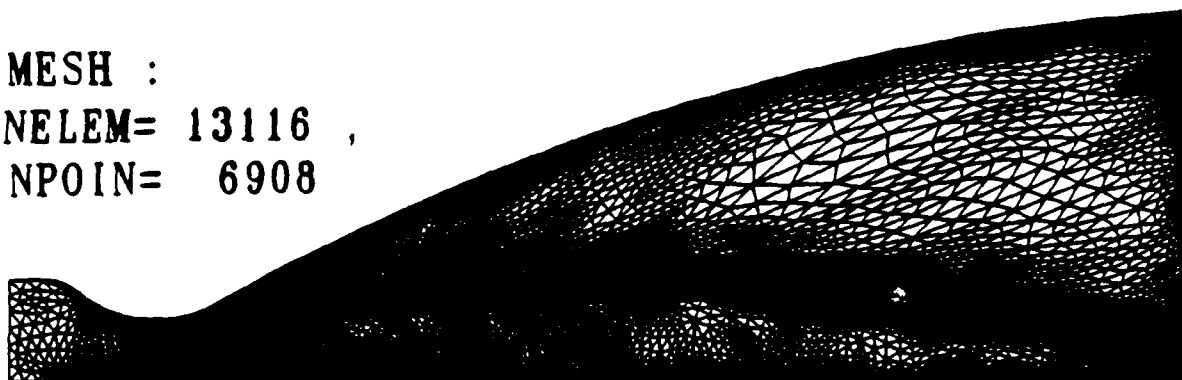


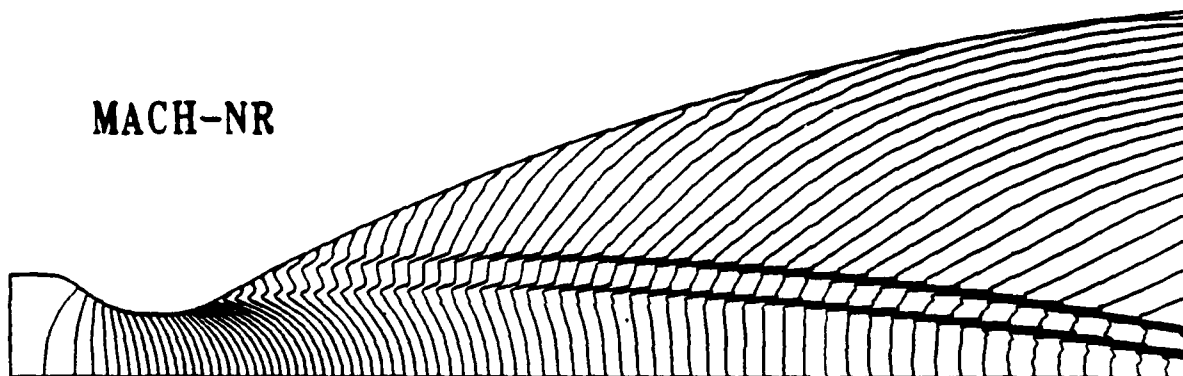
Figure 3h: Shock-Concave Body Interaction: Pressure History at Station 7



MESH :
NELEM= 13116 ,
NPOIN= 6908



MACH-NR



MACH-NR

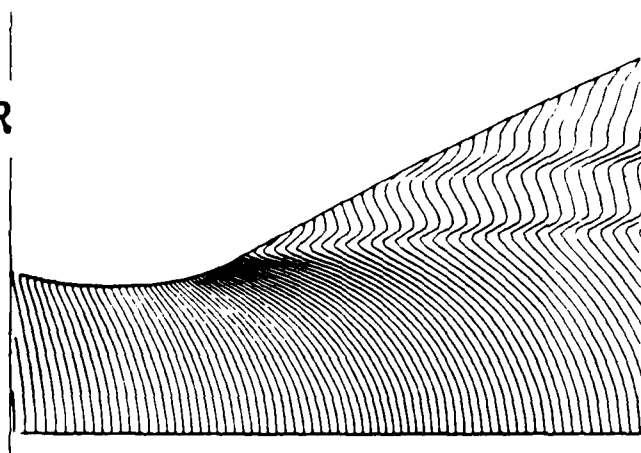


Fig 4. Mesh (a) and Mach Number Contours (b) for the Whole Nozzle and Expanded Mach Number Contours near the Throat.

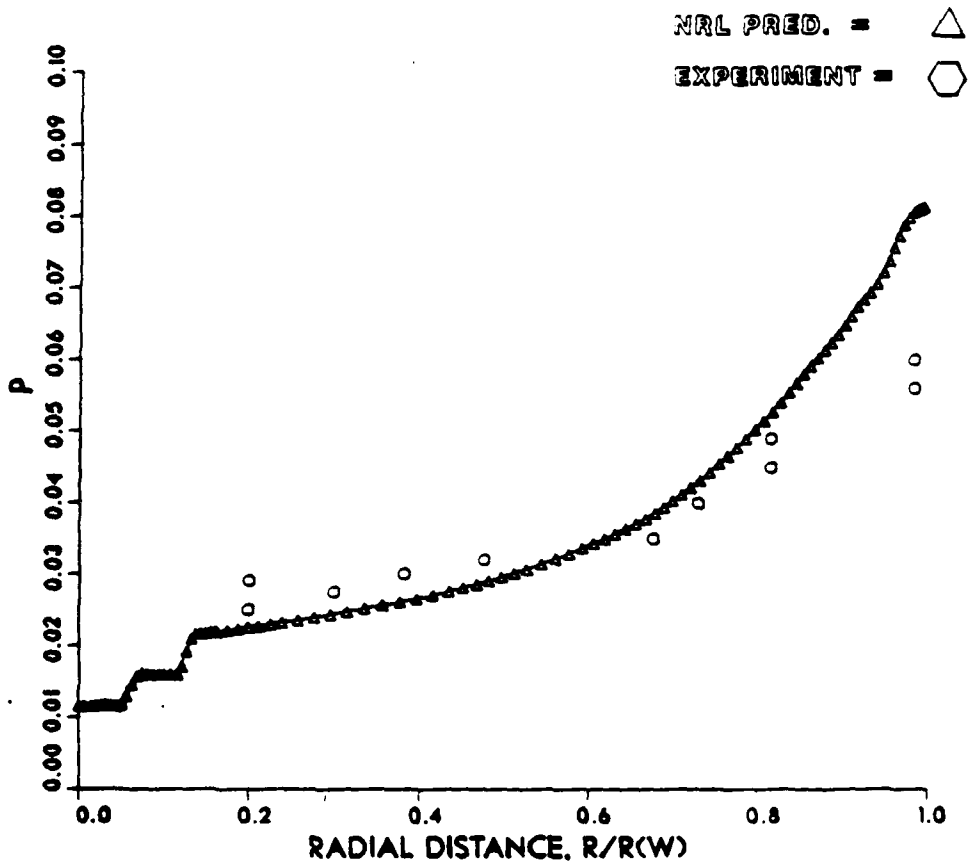
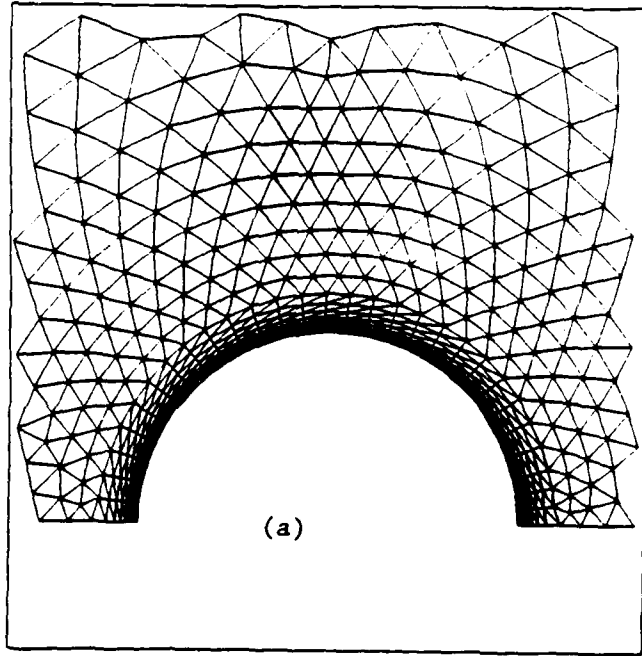
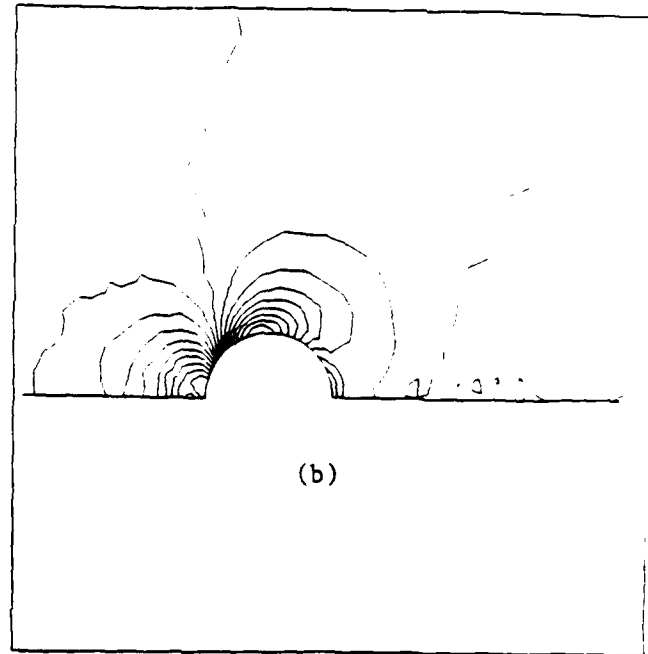


Fig 5. Radial Distribution of Pressures at the Exit Plane; Comparison between Prediction and Experimental Data.

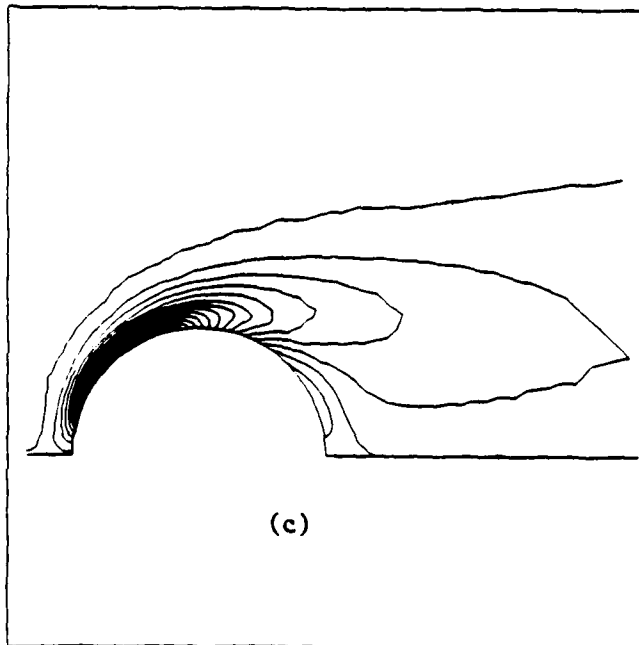
MESH : NELEM= 2029 , NPOINT= 1078



PRESSURE MIN= 0.71E+02 , MAX= 0.72E+02 , DUC= 0.37E+01



VORTICITY : MIN=-0.90E+01 , MAX= 0.96E+00 , DUC= 0.53E+00



VELOCITY VECTORS

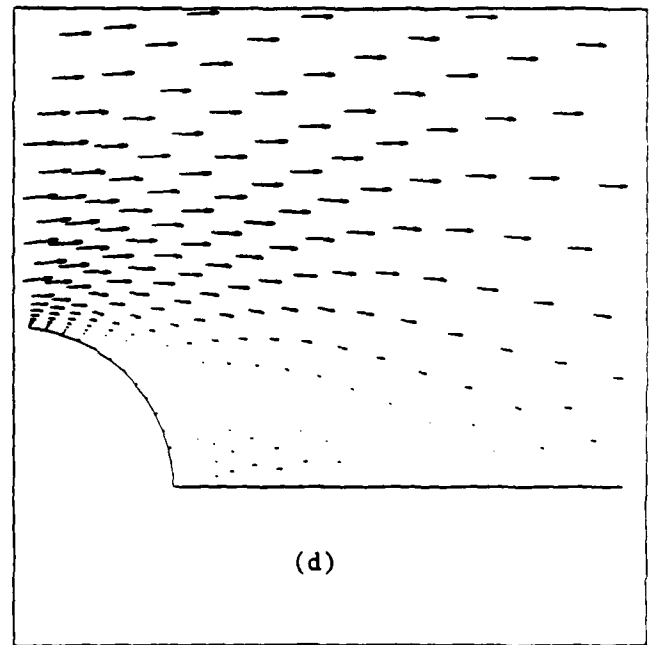


Figure 2. Results for Flow past a Sphere, $Re = 100$.

- (a) Grid;
- (b) Pressure Contours;
- (c) Vorticity Contours;
- (d) Velocity Vectors.

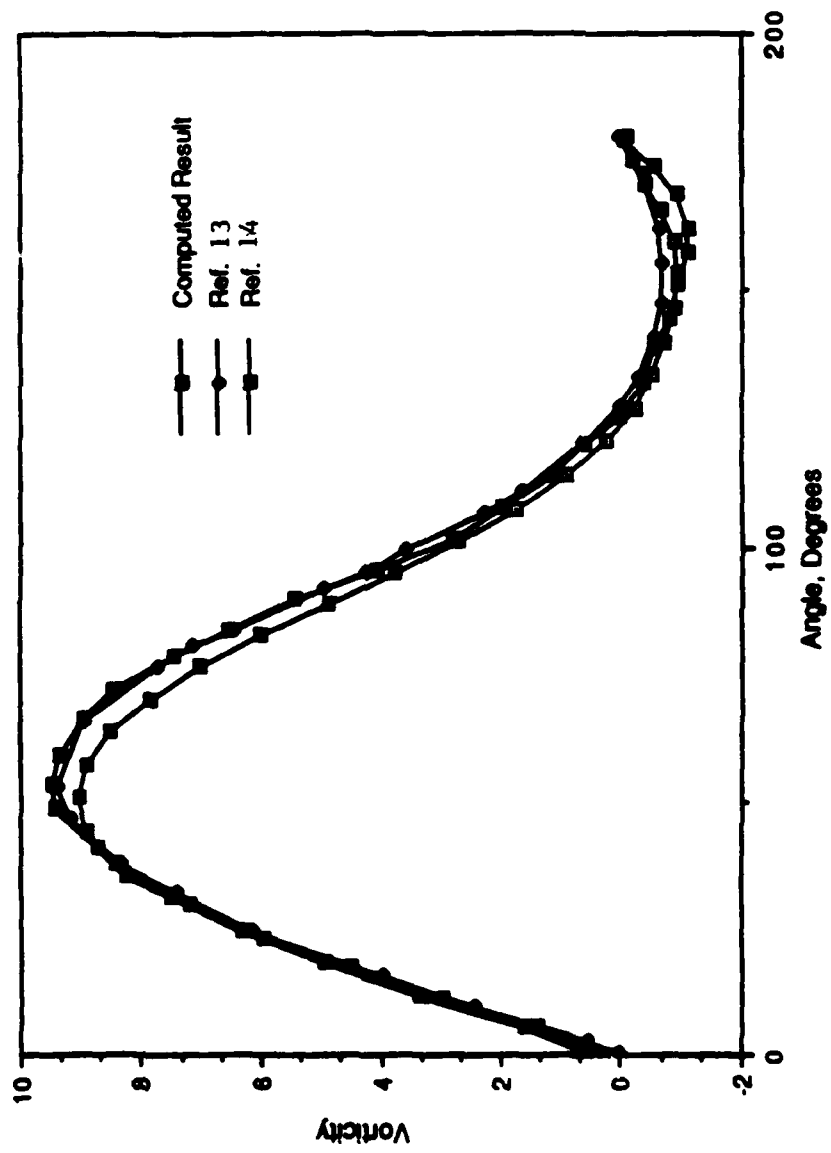


Figure 3. Comparison of Surface Vorticity Distribution on a Sphere.

APPENDIX C

Study of Three-Dimensional Flows Past Complex Geometries Using a Finite-
Element Method

Study of Three-Dimensional Flows Past Complex Geometries Using a Finite-Element Method,*

R. Ramamurti, SAIC & NRL and R. Löhner GWU - The finite-element method of Löhner¹ has been advanced to study the flow past complex 3-D geometries. In the present investigation, the advancing front algorithm² is employed to generate the unstructured grids over a complete submarine configuration. A two-step Taylor-Galerkin procedure is used to discretize the Euler equations of motion. The procedure was tested via application to a model problem of inviscid flow past a sphere at $M_\infty = 0.2$. Comparison of the surface pressure distribution with potential flow is very good. The procedure is then extended for the simulation of 3-D flow past a submarine hull configuration and the results are compared with the axisymmetric solution. Flow past this configuration with sail and stern appendages is also investigated for various pitch angles of attack to study the asymmetric flow properties.

* This work is supported by Naval Research Laboratory under a contract from DARPA.

¹ Löhner, R., Morgan, K. and Zienkiewicz, O.C., Int. J. Num. Meth. Fluids, No.4, 1984.

² Löhner, R. and Parikh, P., AIAA Paper No. 88-0515, 1988.

APPENDIX D

Simulation of Subsonic Viscous Flows Using Unstructured Grids and a Finite
Element Solver

SIMULATION OF SUBSONIC VISCOUS FLOWS USING UNSTRUCTURED GRIDS AND A FINITE ELEMENT SOLVER

Ravi Ramamurti

Science Applications International Corporation, McLean, VA 22102

Rainald Löhner

CMEE, School of Engineering and Applied Science
The George Washington University, Washington, D.C. 20052

Abstract for the 28th Aerospace Sciences Meeting,
Reno, NV, January 1990.

Abstract

A finite element scheme [1-4] has been advanced for solving the Euler and Navier-Stokes equations with unstructured grids in both Cartesian and axisymmetric coordinate systems. A two-step Taylor-Galerkin procedure is employed to discretize the governing equations. The accuracy of the scheme is validated by comparing computed results for flow over a sphere with well known numerical results and via a grid-refinement study for an inviscid flow over an axisymmetric body. The procedure is extended to solve three-dimensional flows over submarine configurations with sail and stern appendages. Convergence acceleration for viscous flows by sub-stepping of the viscous terms is investigated.

Introduction

Numerical solution of flow past complex geometries is an important tool for a fluid dynamicist. The use of finite element methods using unstructured grids for problems involving high speed flows can be found in literature [1-4]. The advantage of using triangular or tetrahedral meshes over structured meshes is that complex geometries can be easily represented. For example, constructing a structured mesh around a submarine with all its appendages requires a tedious task of decomposition of the domain. In this work, unstructured grids are generated using the advancing front algorithm [5].

Most of the conservative schemes which are extensions of 1-D schemes to 2-D and 3-D through operator splitting, cannot be employed with unstructured grids, as the discretization stencils obtained on these grids are inherently multidimensional. The high resolution scheme employed in the present study is based on Zalesak's [6] generalization of the Flux-Corrected Transport (FCT) algorithm of Boris and Book [7].

Governing Equations

The equations governing the fluid flow are the Navier-Stokes equations, and can be written as

$$\frac{\partial U}{\partial t} + \frac{\partial F_a^x}{\partial x} + \frac{1}{r^j} \frac{\partial F_a^r}{\partial r} + k \frac{\partial F_a^z}{\partial z} = j \frac{S_a}{r} + \frac{\partial F_v^x}{\partial x} + \frac{1}{r^j} \frac{\partial F_v^r}{\partial r} + k \frac{\partial F_v^z}{\partial z} + j \frac{S_v}{r} \quad (1)$$

$j = 1, k = 0$: axisymmetric case

$j = 0, k = 1$: 3-dimensional case

where $U = (\rho, \rho u, \rho v, \rho e)^T$

and F_a and F_v are inviscid and viscous fluxes respectively.

The equation of state for an ideal polytropic gas can be written as

$$p = (\gamma - 1) \rho \left[e - \frac{1}{2} [(\rho u)^2 + (\rho v)^2] \right]. \quad (2)$$

For the axisymmetric case the system of Eqs. (1) is multiplied with r to yield

$$\frac{\partial(rU)}{\partial t} + \frac{\partial(rE)}{\partial x} + \frac{\partial F}{\partial r} = S_a + \frac{\partial(rE_v)}{\partial x} + \frac{\partial F_v}{\partial r} + S_v, \quad (3)$$

Using this form of the conservative equations can be shown to be the same as integrating the system of Eqs. (1) in a consistent manner. Moreover, the use of conservative form represented by Eq. (3) in conjunction with separate interpolations for r and U avoids the problems encountered for $r = 0$ using a node-centered scheme.

Two-Step Taylor-Galerkin Procedure

The two-step Taylor-Galerkin algorithm has been used extensively for the computation of both inviscid and viscous flows in two and three dimensions for Cartesian coordinate systems [2-4]. Given a system of partial differential equations of the form:

$$\frac{\partial U}{\partial t} + \frac{\partial F_a^i}{\partial x^i} = S_a + \frac{\partial F_v^i}{\partial x^i} + S_v, \quad (4)$$

where U, F_a^i and S_a denote the vector of unknowns, advective fluxes and advective source terms, and F_v^i and S_v denote viscous fluxes and viscous source terms, we proceed as follows:

a) First step (Advective predictor):

$$U^{n+\frac{1}{2}} = U^n + \frac{\Delta t}{2} \cdot (S_a|^n - \frac{\partial F_a^i}{\partial x^i}|^n) \quad (5)$$

b) Second step :

$$\Delta U^n = U^{n+1} - U^n = \Delta t \cdot (S_a|^{n+\frac{1}{2}} - \frac{\partial F_a^i}{\partial x^i}|^{n+\frac{1}{2}} + \frac{\partial F_v^i}{\partial x^i}|^n + S_v|^n) . \quad (6)$$

In both substeps the spatial discretization is performed via the usual Galerkin weighted residual method [2-4]. However, we note that at $t^{n+\frac{1}{2}} = t^n + \frac{1}{2}\Delta t$, the quantities U, F, S are assumed piecewise constant, whereas at t^n, t^{n+1} , the quantities U, F, S are assumed piecewise linear.

Convergence Acceleration

A Fourier stability analysis for the explicit scheme described above, shows that the scheme is stable provided

$$C \leq \frac{\sqrt{1 + Re_\Delta} - 1}{Re_\Delta} \quad (7)$$

where C is the Courant number and Re_Δ is the minimum cell Reynolds number. Convergence to steady state can be accelerated by local timestepping. Although this local time-stepping strategy is efficient for inviscid flows, convergence is rather poor for viscous flows. Hence, a sub-stepping of the viscous terms is investigated. This involves advancing the inviscid fluxes with their maximum allowable Δt and computing the corresponding right hand side. This inviscid time-step is divided into a given number of viscous sub-steps. The contribution from the viscous terms to the right hand side is then computed and added to the corresponding fraction of the inviscid right hand side. Complete details of this procedure will be given in the final version of the paper.

Results

Axisymmetric Flow

Flow past a Sphere, $Re=100$ (steady, viscous)

Steady viscous flow past a sphere at a Mach-number of $M_\infty = 0.1$ and Reynolds-number of $Re = 100$ provides an important test example to evaluate the accuracy of the present scheme. No artificial viscosity was added for this subsonic case. The problem statement, as well as the results obtained, are shown in Figure 1. The grid employed for this case (Fig. 1a) consists of a structured portion divided into triangles in the boundary layer zone, and an unstructured mesh elsewhere. From Fig. 1d, it can be seen that the recirculation zone extends 1.4 diameters into the wake, measured from the center of the sphere. This compares well with experimental results [9]. Figure 1e shows very good agreement of computed surface vorticity with earlier numerical results [10,11]. The flow separates at an angle of approximately 123° .

Flow past a Body of Revolution at Zero Angle of Attack

Having established the correctness of the procedure, the present scheme was applied to solve flow past a hull-shaped body of revolution. First, the inviscid equations were solved on a coarse grid consisting of 988 points and 1807 elements. The results for $M_\infty = 0.2$, are shown in Fig. 2. In order to establish the reliability of the solutions, a grid refinement study is undertaken. The grid was refined using the classic h-refinement technique. The results in terms of pressure contours and velocity vectors are shown in Fig. 3. Figure 4 shows the comparison of the surface pressure distribution, obtained employing the two grids. One can see that the effect of grid refinement is minimal on the quality of the solution. This indicates that the first mesh was already quite adequate.

Next, the procedure was applied to solve steady viscous flow past this configuration at $M_\infty = 0.1$ and $Re = 1000$. The grid employed for this case consists of 7276 nodes and 14093 elements, and is shown in Fig. 5a. Results in terms of pressure and vorticity contours and velocity vectors are shown in Fig 5b-d. Correct trend in surface pressure distribution is observed. The vorticity contours show a tendency for the flow to separate in the afterbody region. This solution was obtained with local time-stepping but without sub-stepping of the viscous terms. Convergence, defined by reduction of residuals by three orders of magnitude, was achieved in 5000 steps. Convergence acceleration for this case is currently being pursued.

3-Dimensional Flow

Inviscid Flow Past a Sphere, $M_\infty = 0.2$

Next, the procedure was extended to 3-D and an inviscid flow past a sphere was chosen as the test case, since axisymmetric results from the present study and earlier results are available for this case. Figure 6a shows the comparison of the surface pressure distribution. From this figure, it is clear that the axisymmetric case compares very well with the potential flow solution; the agreement of the 3-D solution is fairly good except near the two stagnation points. This discrepancy may be due to the small artificial dissipation that was needed to stabilize the 3-D solution procedure. Figure 6b shows the pressure contours over the surface of the sphere.

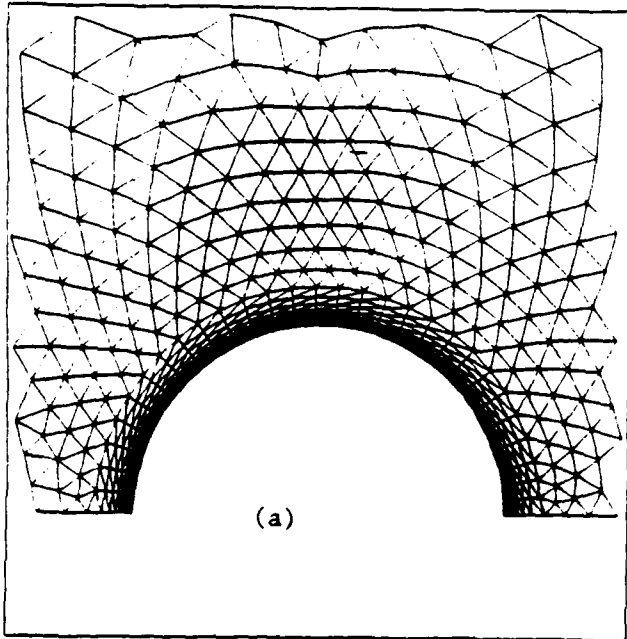
Inviscid Flow Past a Fully Appended Submarine

The procedure was extended to solve inviscid flow past a submarine with sail and stern appendages, at a Mach number $M_\infty = 0.2$ and a pitch angle of attack of 10° . The grid employed for this case consists of 410,162 tetrahedra and 71,524 nodes and is shown in Fig. 7a. Convergence to steady state was achieved in 800 iterations, and the results in terms of surface pressure contours is shown in Fig. 7b. Currently, unsteady viscous simulation of flow around this configuration is being pursued, and will be presented in the final version of the paper.

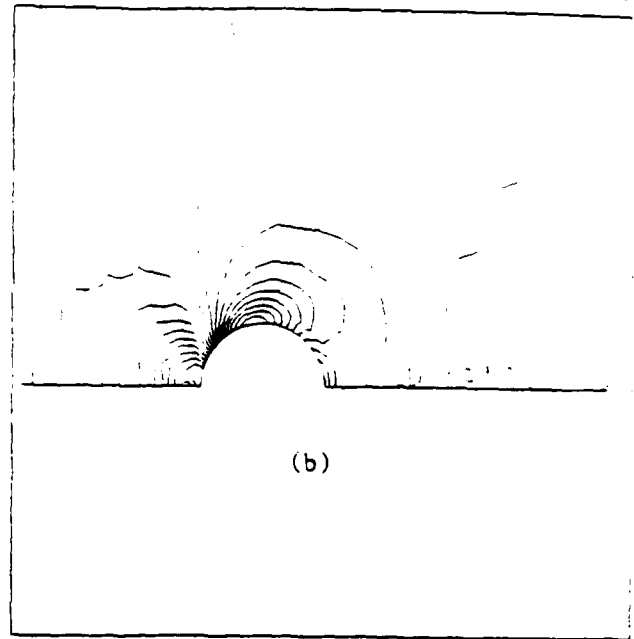
References

- [1] Löhner, R., Morgan, K. and Zienkiewicz, O.C., "The Solution of Non-linear Systems of Hyperbolic Equations by the Finite Element Method," *Int.J.Num.Meth.Fluids*, No. 4, pp. 1043-1063, 1984.
- [2] Löhner, R., Morgan, K., Peraire, J. and Zienkiewicz, O.C., "Finite Element Methods for High Speed Flows," *AIAA-CP 85-1531*, 1985.
- [3] Löhner, R., Morgan, K. and Zienkiewicz, O.C., "An Adaptive Finite Element Procedure for High Speed Flows," *Comp. Meth. Appl. Mech. Eng.* Vol. 51, pp. 441-465, 1985.
- [4] Löhner, R., Morgan, K., Peraire, J. and Vahdati, M., "Finite Element Flux-Corrected Transport (FEM-FCT) for the Euler and Navier-Stokes Equations," *ICASE Rep. 87-4*, *Int.J.Num.Meth. Fluids* 7, pp. 1093-1109, 1987.
- [5] Löhner, R. and Parikh, P., "Generation of Three Dimensional Unstructured Grids by the Advancing Front Method," *AIAA Paper No. 88-0515*, January 1988.
- [6] Zalesak, S.T., "Fully Multidimensional Flux-Corrected Transport Algorithm for Fluids," *Journal of Computational Physics*, Vol. 31, pp. 335-362, 1979.
- [7] Boris, J.P. and Book, D.L., "Flux-Corrected Transport. III. Minimal- Error FCT algorithms," *Journal of Computational Physics*, Vol. 20, pp. 397-431, 1976.
- [8] Löhner, R., Morgan, K. and Peraire, J., "A Simple Extension to Multidimensional Problems of the Artificial Viscosity due to Lapidus," *Comm.Appl.Num.Meth.*, Vol. 1, pp. 141-147, 1985.
- [9] Van Dyke, M., "An Album of Fluid Motion," *Parabolic Press*, 1982.
- [10] Clift, R., Grace, J.R. and Weber, M.E., "Bubbles, Drops and Particles," *Academic Press*, 1978.
- [11] Rimon, Y. and Cheng, S.I., "Numerical Solution of a Uniform Flow over a Sphere at Intermediate Reynolds Numbers," *The Physics of Fluids*, Vol. 12, No. 5, 1969.

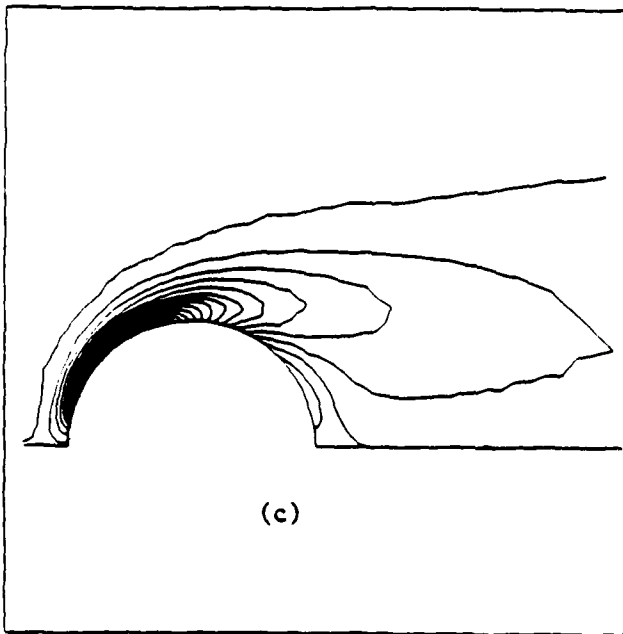
MESH NELEM= 2029 . NPQIN= 1078



PRESSURE MIN= 0.71E+02 . MAX= 0.70E+02 . DUC= 0.37E+01



VORTICITY MIN=-0.90E+01 . MAX= 0.96E+00 . DUC= 0.53E+00



VELOCITY VECTORS

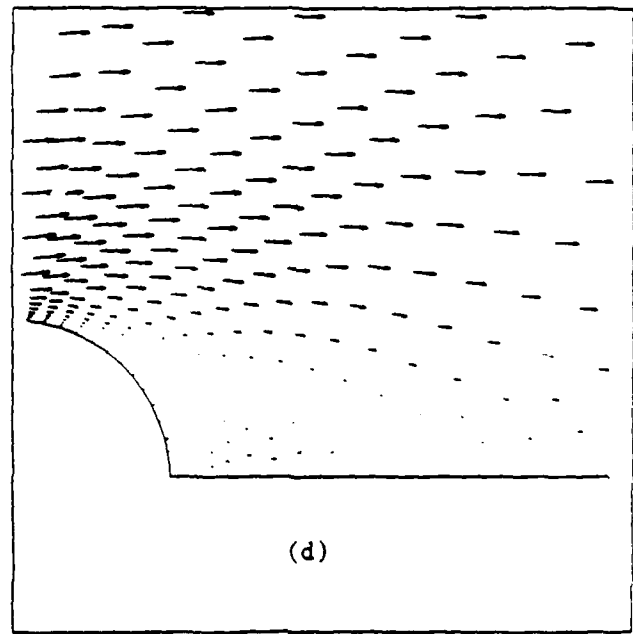


Figure 1. Results for Flow past a Sphere, $Re = 100$.

- (a) Grid;
- (b) Pressure Contours;
- (c) Vorticity Contours;
- (d) Velocity Vectors.

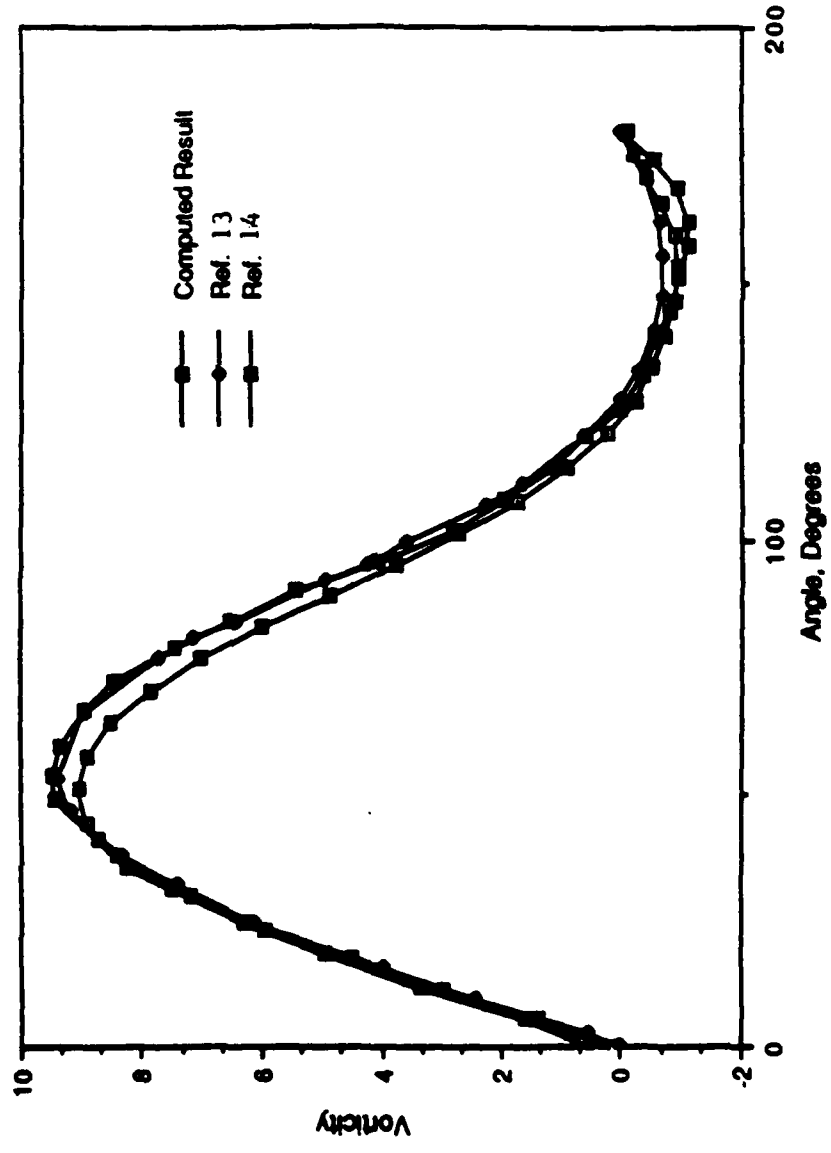
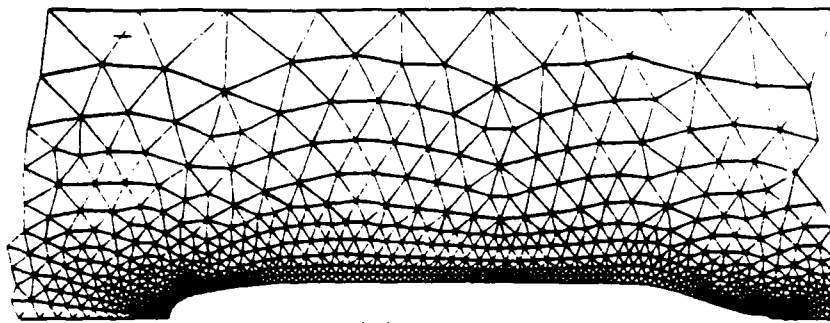


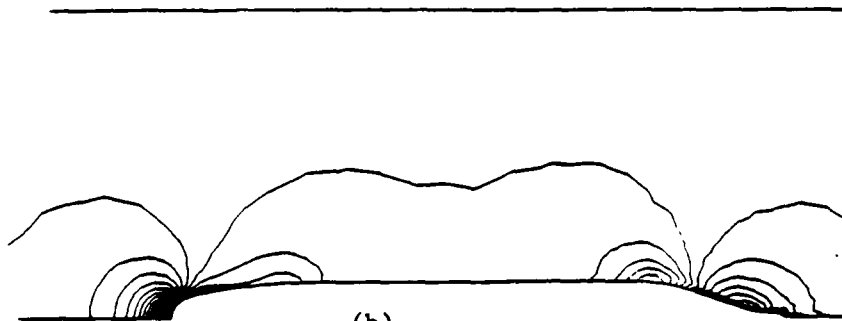
Figure 4e Comparison of Surface Vorticity Distribution on a Sphere.

MESH NELEM= 1807 . NP0IN= 998

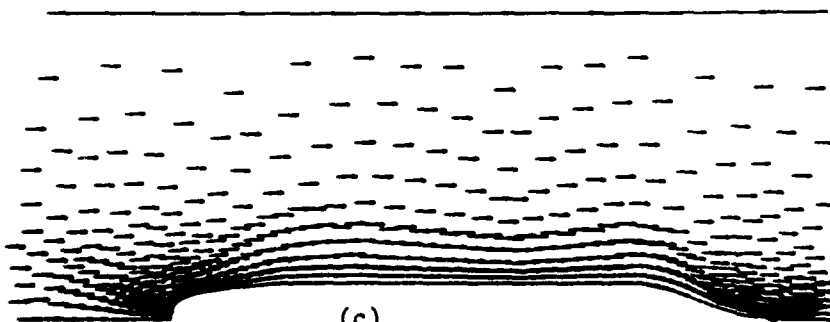


(a)

PRESSURE: MIN= 0.13E+02 . MAX= 0.18E+02 . DUC= 0.20E-01



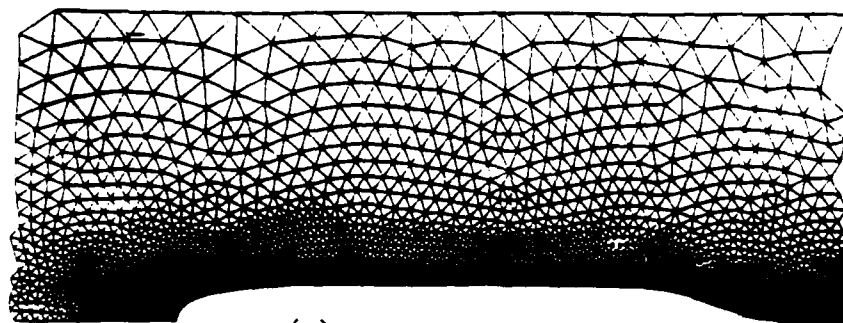
(b)



(c)

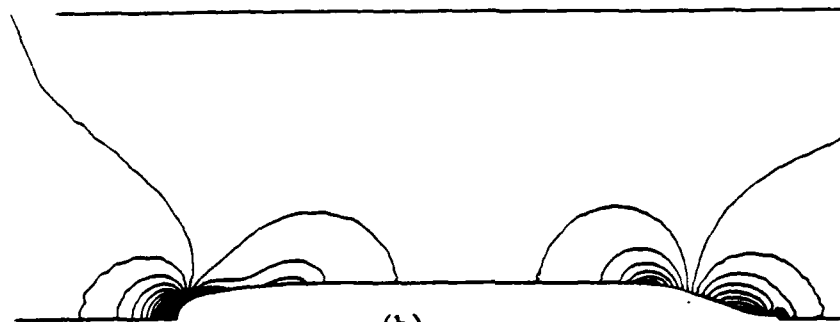
Figure 2 Results for Flow past a Hull, $M_\infty = 0.2$, Coarse Mesh.
(a) Grid; b) Pressure Contours; (c) Velocity Vectors.

MESH NELEM= 7228 . NP0IN= 3802

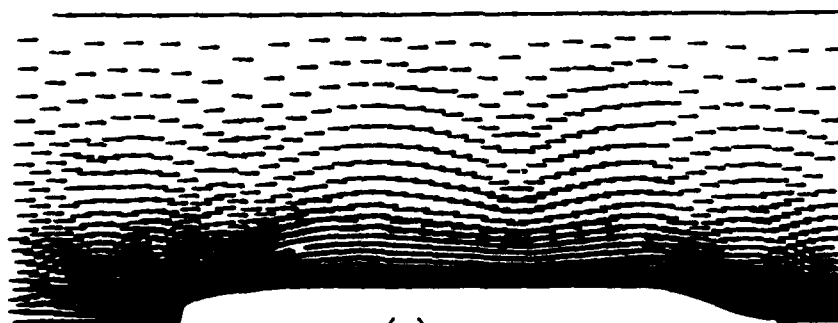


(a)

PRESSURE MIN= 0.18E+02 . MAX= 0.19E+02 . DUC= 0.20E-01



(b)



(c)

**Figure 3 Results for Flow past a Hull, $M_\infty = 0.2$, Fine Mesh.
(a) Grid; (b) Pressure Contours; (c) Velocity Vectors.**

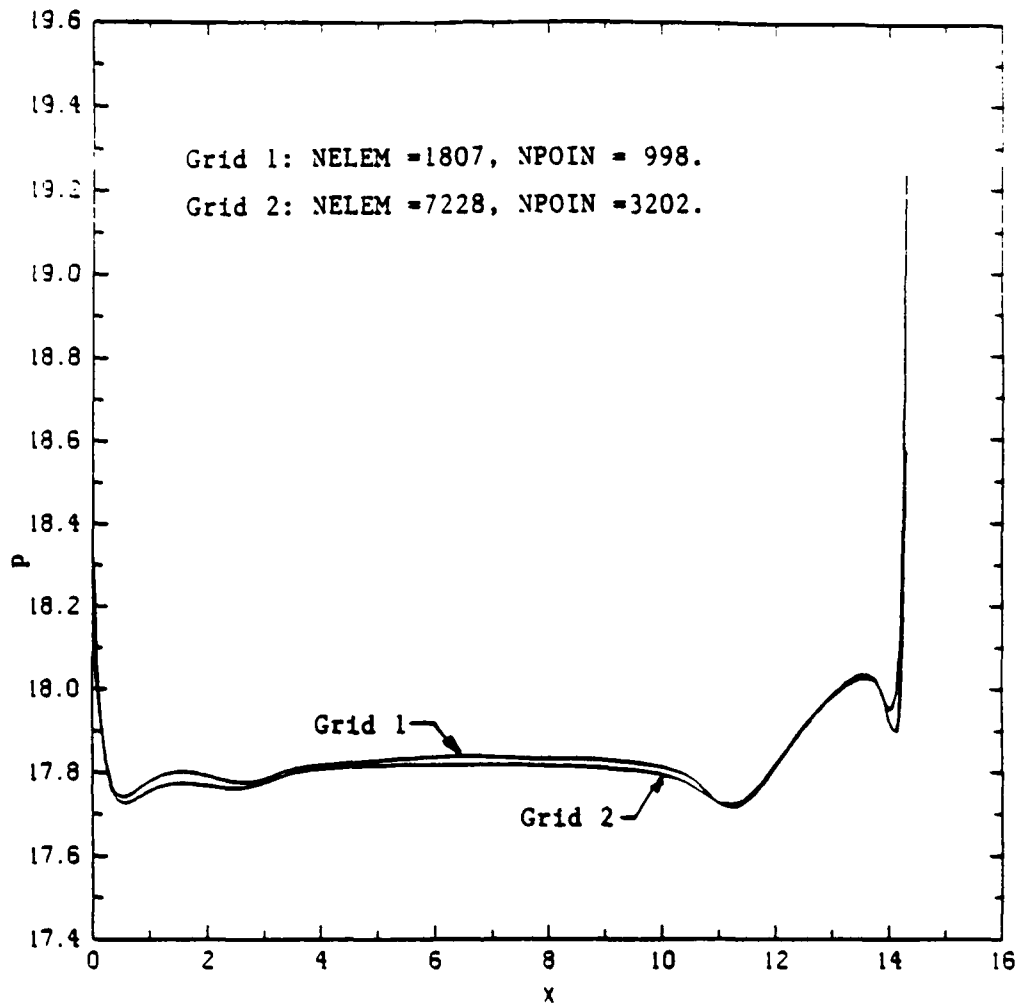


Figure 4 Effect of Grid Refinement on the Surface Pressure.

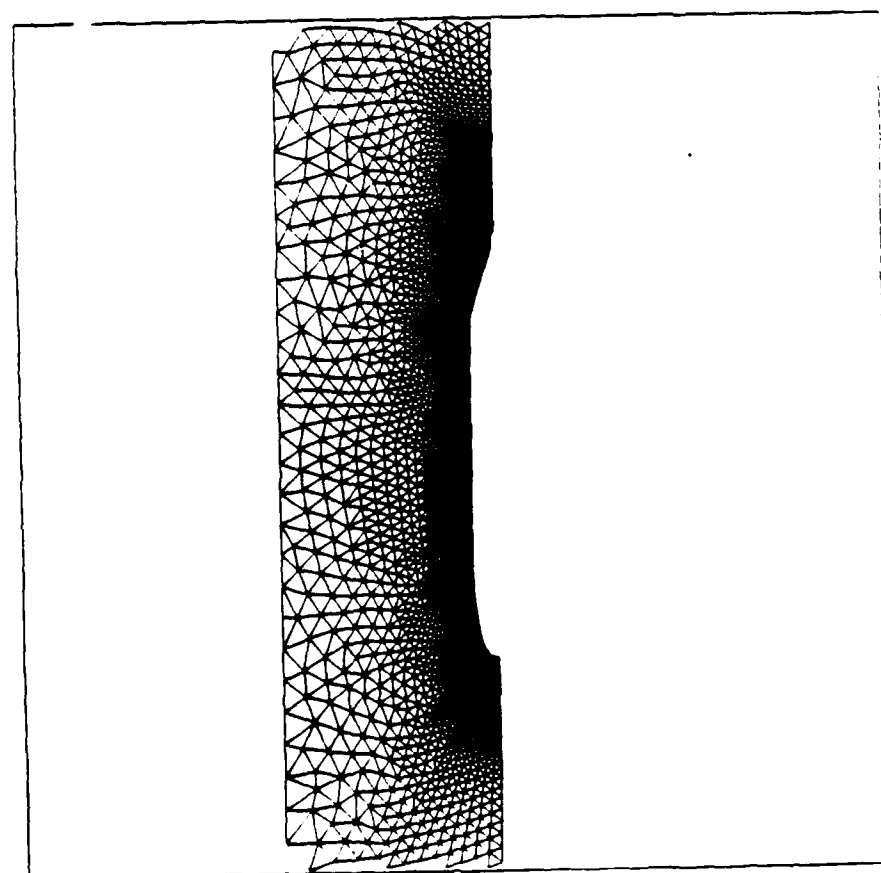
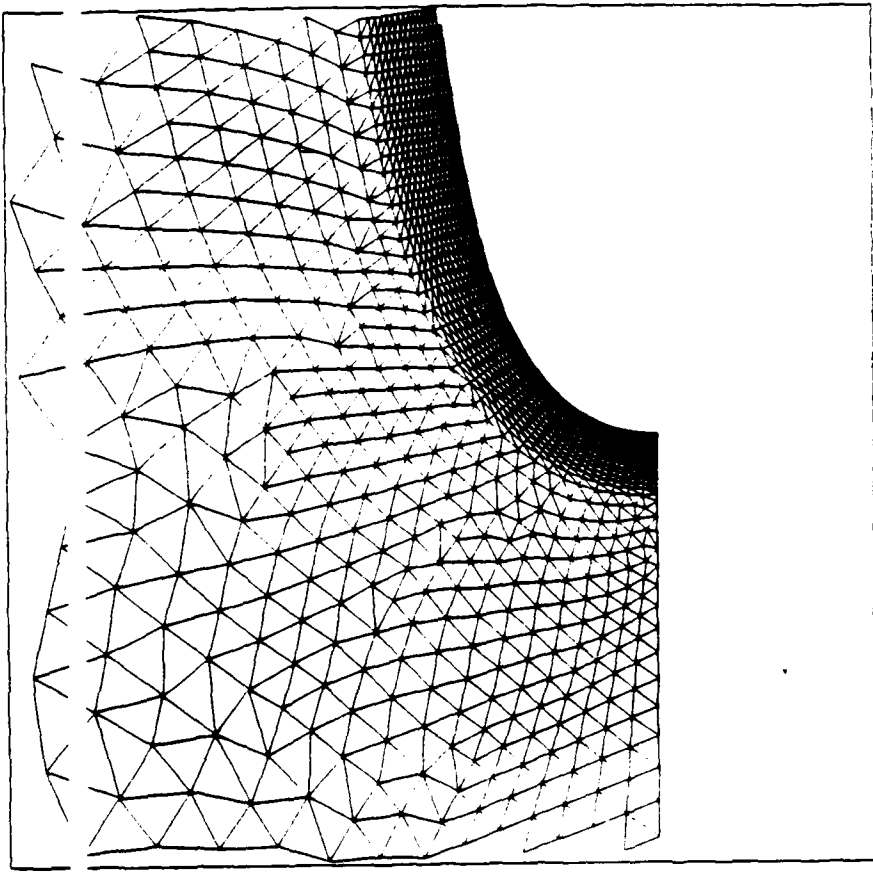


Figure 5a: Mesh employed for the viscous case.

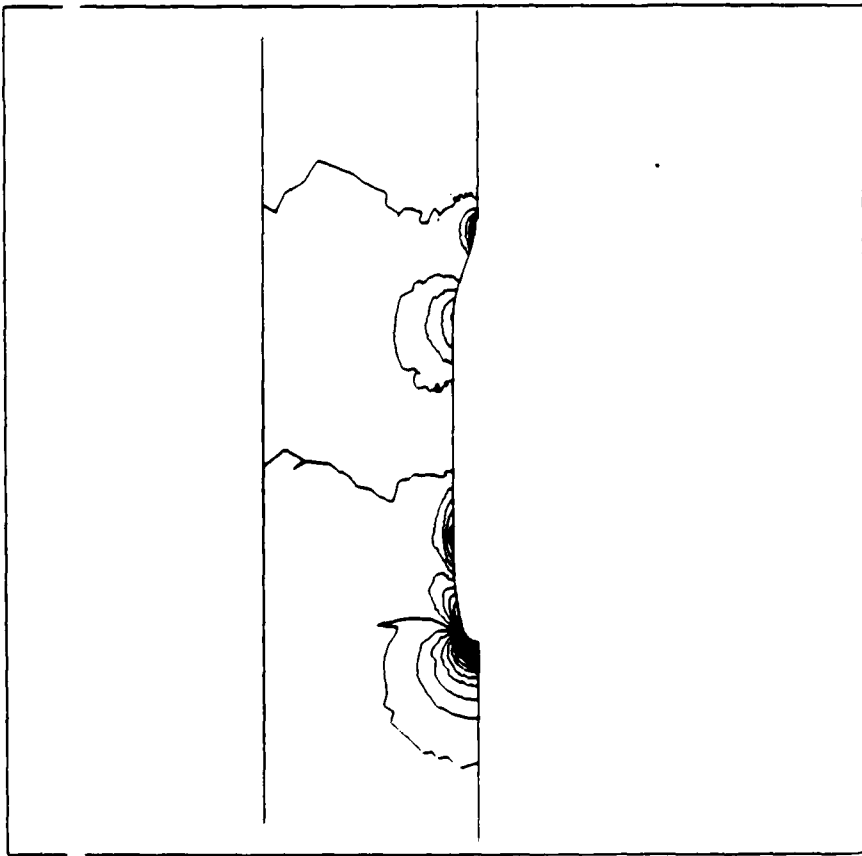


Figure 5b: Pressure

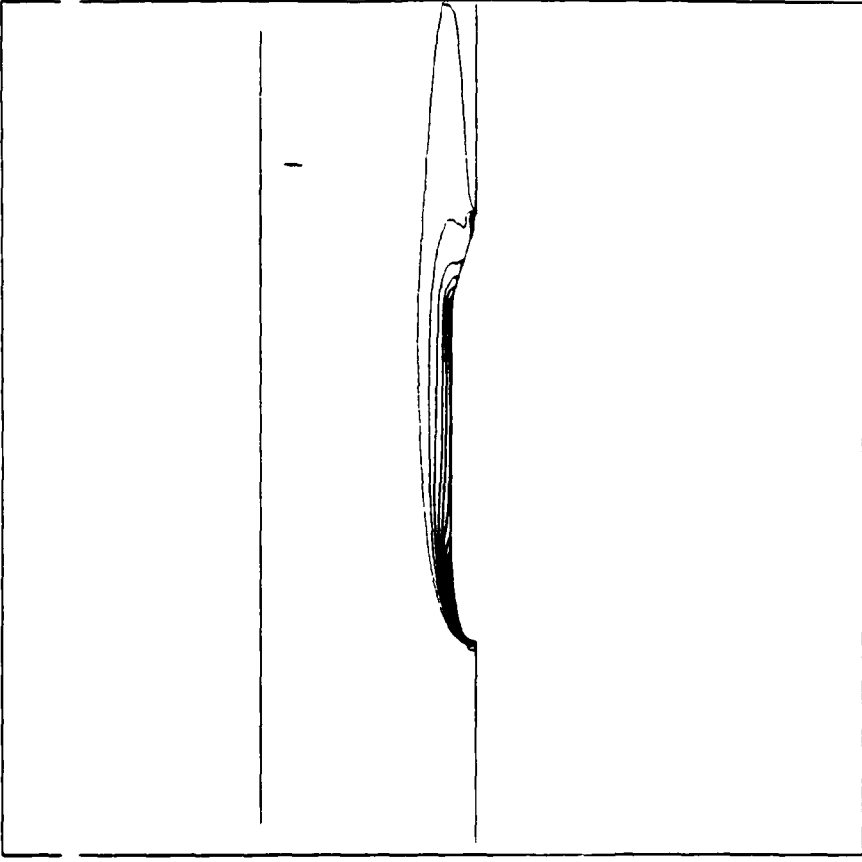


Figure 5c: Vorticity

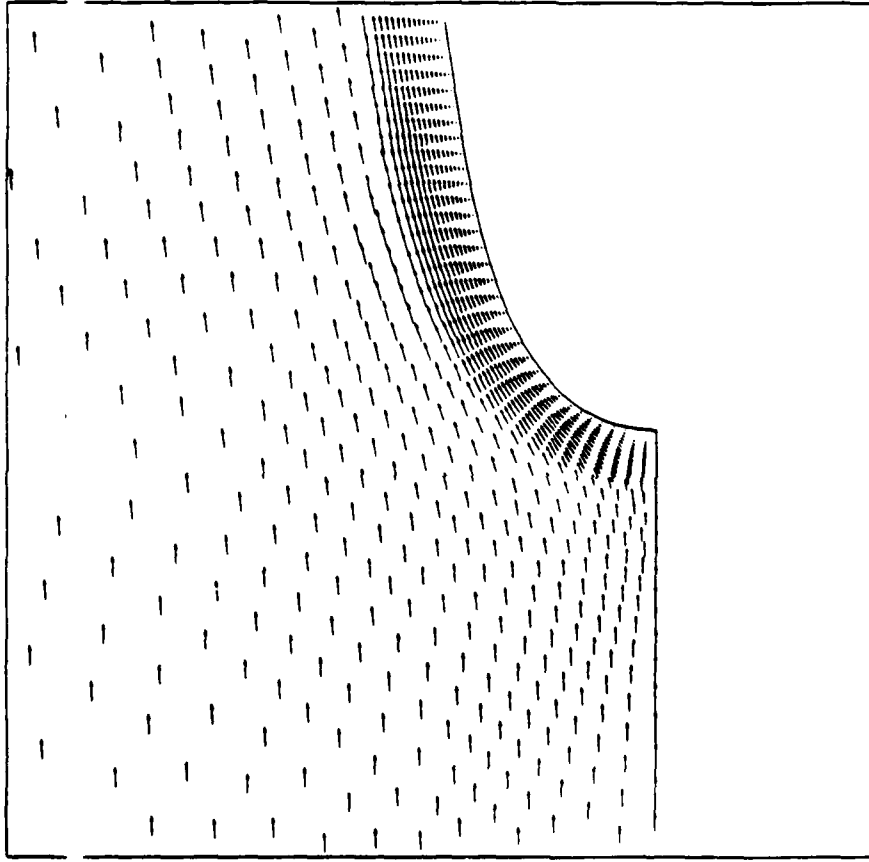


Figure 5d: Velocity Vectors in the Front Stagnation Region

SURFACE PRESSURE DISTRIBUTION

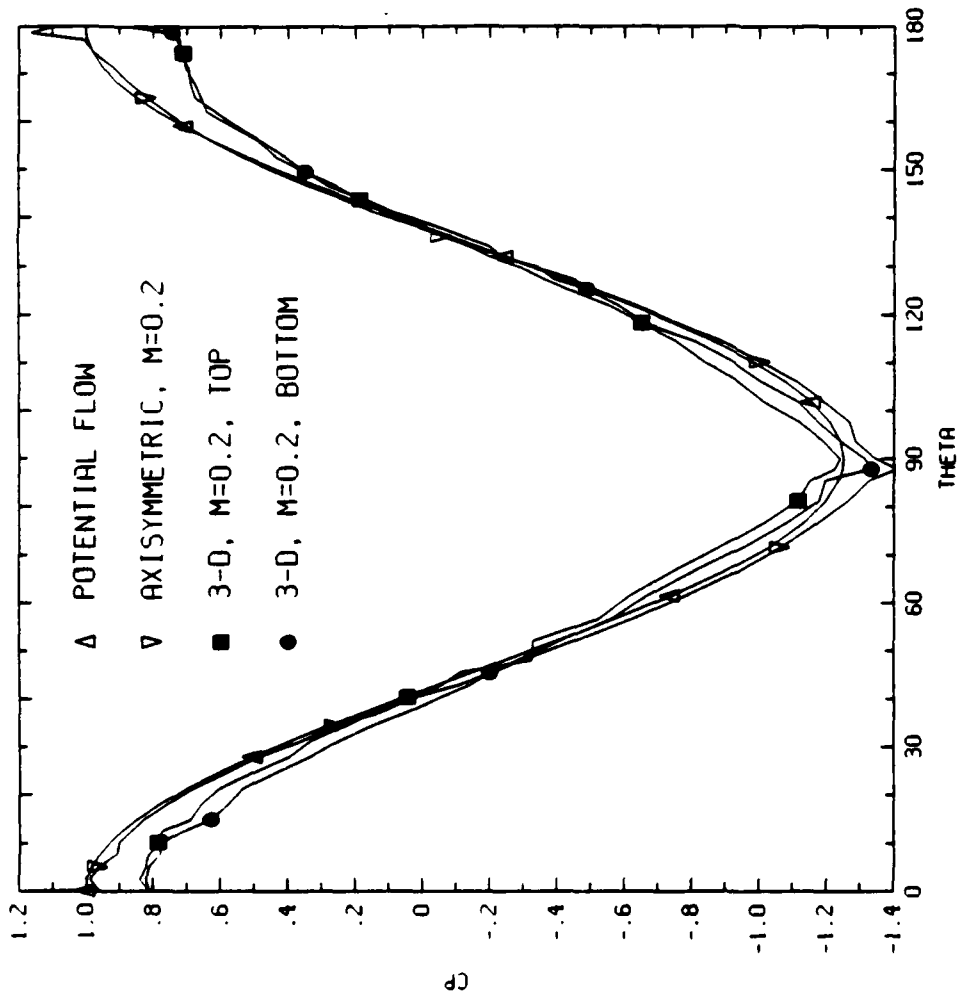


Figure 6a: Inviscid Flow past a Sphere: Axisymm./3-D Pressure

PRESSURE
 1.826E+01
 1.822E+01
 1.818E+01
 1.814E+01
 1.810E+01
 1.806E+01
 1.803E+01
 1.799E+01
 1.795E+01
 1.791E+01
 1.787E+01
 1.783E+01
 1.779E+01
 1.775E+01
 1.771E+01
 1.767E+01
 1.763E+01
 1.759E+01
 1.755E+01
 1.751E+01
 1.747E+01
 1.743E+01
 1.739E+01
 1.735E+01
 1.731E+01
 1.727E+01
 1.723E+01
 1.719E+01
 1.715E+01
 1.711E+01
 1.707E+01

z ---- M



Figure 6b: Inviscid Flow past a Sphere: Pressure Contours

PRESSURE

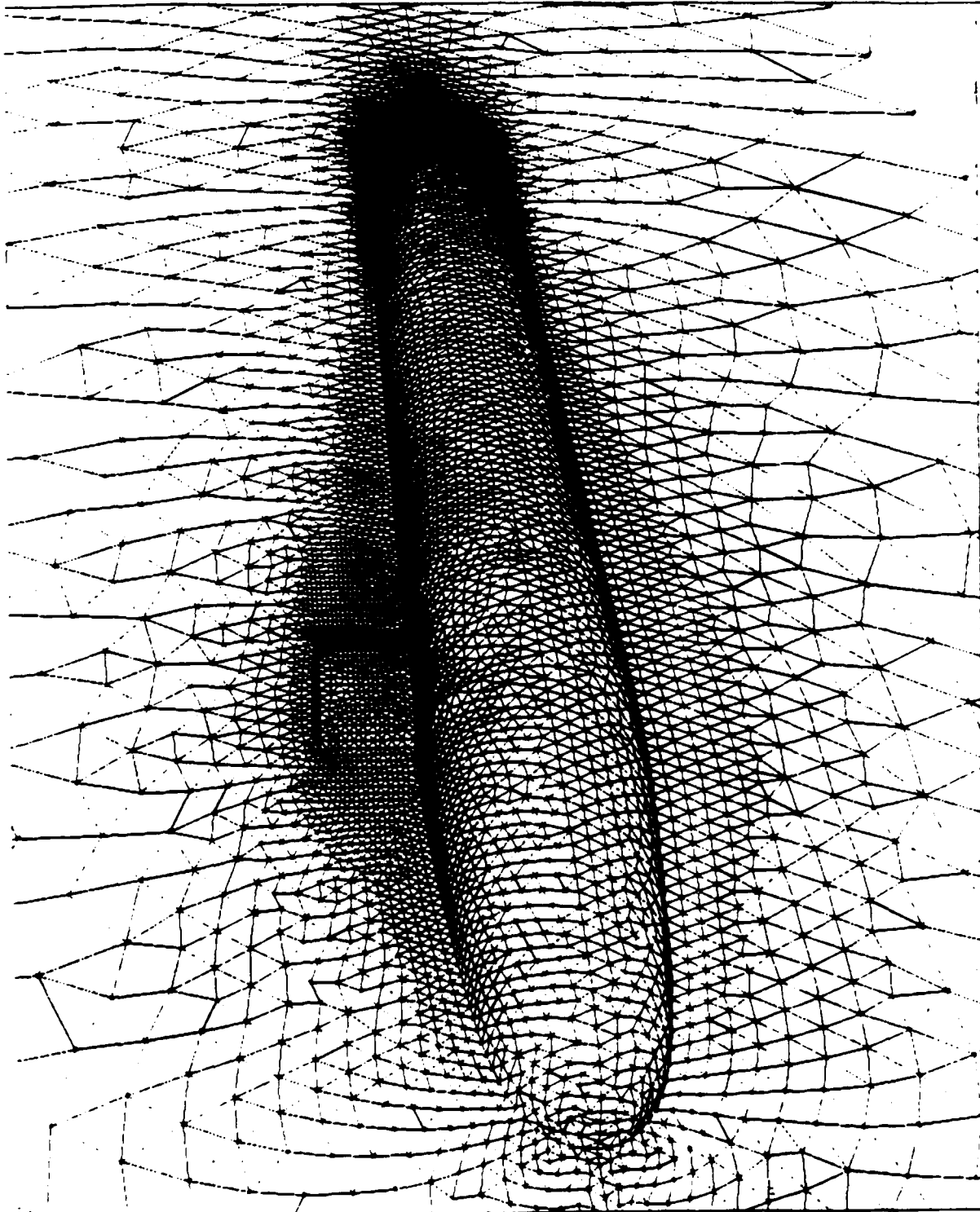


Figure 7a: Fully Appended Submarine: Surface Mesh

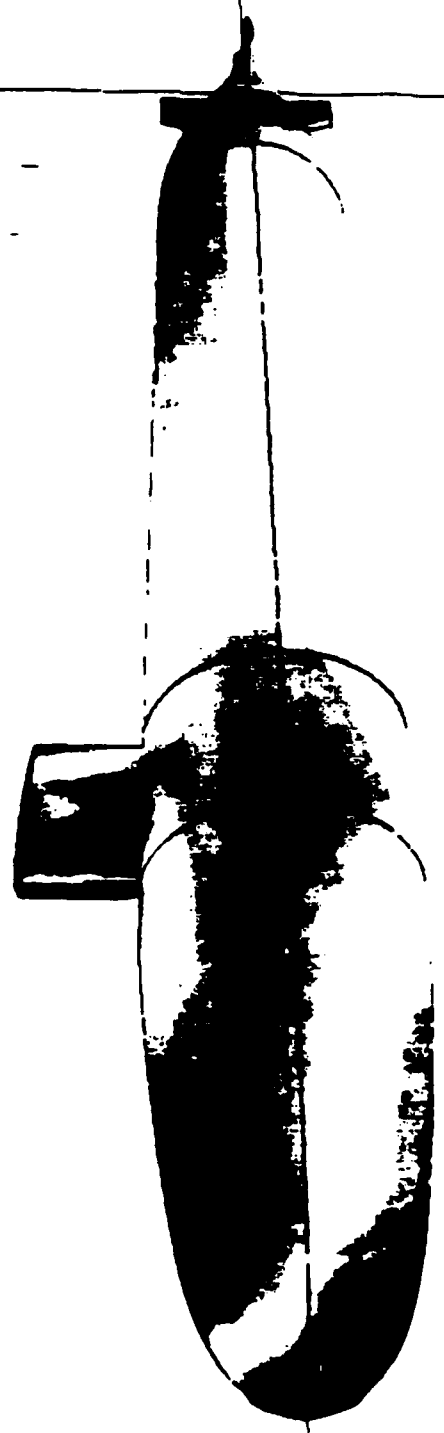
PRE SSURE
 1. 0175J +00
 1. 011M +00
 1. 0311 +00
 1. 027M +00
 1. 026J +00
 1. 024E +00
 1. 022E +00
 1. 020E +00
 1. 018E +00
 1. 016J +00
 1. 013H +00
 1. 011J +00

9. 0175J -01
 9. 011M -01
 9. 0311 -01
 9. 027E -01
 9. 026E -01
 9. 024E -01
 9. 022E -01
 9. 020E -01
 9. 018E -01
 9. 016J -01
 9. 013H -01
 9. 011J -01

— 2

PRE SSURE

Figure 7b: Fully Appended Submarine: Pressures on the Surface



APPENDIX E

Algorithms for Improved Gating Combinatorics in Multitarget Tracking

Algorithms for Improved Gating Combinatorics in Multitarget Tracking

Miguel R Zuniga*
Science Applications International Corporation
1710 Goodridge Dr.
McLean, VA, 22102

August 9 , 1989

I. Introduction

Multitarget tracking algorithms have appeared in recent literature [1,2,3]. Reference 1 provided an analysis of the scaling of times of possible combinatorial bottlenecks, e.g. gating, hypothesis generation, and cluster merging. Suggestions were made for improving scaling and/or the speed of each. In this report we focus on scaling and speed improvements of gating algorithms, whose combinatorial problem we define as follows: given a set of N_r observations and N_t tracks, perform a matching algorithm such that we identify all the observation-track pairs, whose scores fall above a certain threshold. For a fixed object density or for a variable density that is sufficiently low, we verify that the overall cost of making pairs will scale as $O(N_r \ln N_t)$. For high density and observation reports with unequal timestamps, we show that the overall cost of making the pairs can be made to scale better than $N_t \ln N_t N_r^{1/(\beta+1)}$, where β is a parameter known as the search dimension and which will be discussed below.

In the next section we present technical terms and definitions. In section III. we describe the problem in greater generality. We treat two cases: (1) the case with either low object density or all observations made at the same time, and (2) the case of high density and with observations made at different times. In section IV. we show that one can use near neighbors search algorithms for the first case, and we discuss the derivation of a search radius from a pair score threshold. In sections V. and VI. we show how to extend these techniques to the second case, with the aid of an auxiliary algorithm. Scaling analysis is then done for these combined algorithms. In sections VII. and VIII. we give a brief discussion and conclusions respectively.

II. Preliminary Details

By an observation we mean a set whose items are measured simultaneously at some specified time. We call this time the validity time of the observation or the "time-stamp" of the observation. In our discussion and in the simulations we require that

*Laboratory for Computational Physics and Fluid Dynamics, Naval Research Laboratory, Washington, D.C. 20375

the timestamps all be within a period of time called a "scan" of length T_s . For the simulation presented here, the timestamps are of uniform random distribution. A track is an estimate that in some sense converges to the "true trajectory" as the number of observations correctly matched to the track increases. There are β position components to each track at any one time. And, similarly, among the items of an observation there are β position components. When a geometrical position search is done, we use all β components and only these components. In particular, we do not explicitly use the observation validation time for the searches. Also, further information may come with observations, e.g. the location of the measurement device and the extent of its detection volume. This additional information is not used in the techniques presented here, but if used intelligently it could speed the searching.

We define a score for observation-track pair (i, j) as the function:

$$S_{ij}(dR_{ij}, \Gamma_i) \propto \frac{\exp(dR^t \Gamma_j^{-1} dR)}{\det \Gamma_j^{1/2}} \quad (1)$$

where Γ_j is the residual covariance of the track j , and dR is the vector position difference of the pair, and these arguments are taken to be valid at the same time.

In our simulations we use "near-neighbors-within-a-radius" algorithms - the acronym is NRA. The two NRA's we use in this study are: a search tree [4], which in this paper we shall refer to as the "BLD tree"; and a modification of the Ordered Partition [5] which we shall refer to as the "OP". These are the algorithms of choice primarily because of their non statistical nature, i.e. guaranteed to find the near neighbors within a prescribed radius, but also because of their search time scaling.

III. Problem Overview

In the subsequent discussions we assume that we cannot integrate the observations in time. Given a set of N_t tracks and a set of N_r reports, there are at most $N_t N_r$ scores S which can be formed. Of these, only a fraction q of them will fall above the threshold, and q could be as low as $1/N_t$ or $1/N_r$, or smaller. Ideally we would only calculate the $q N_t N_r$ scores and not have any overhead for identifying these correct pairs. At worst we would calculate the $N_t N_r$ scores and, in addition, have significant overhead related to this. An example of a brute force approach is the following technique: assume the reports have different times and so for each report, integrate the equations of motion of the tracks to update all tracks to the time on the report and to calculate N_t scores. For each report, keep those scores that are above the desired threshold. The dominant cost of this is the $O(N_r N_t)$ score calculations and integrations. There are probably many schemes for avoiding the brute force costs. The approach we offer here is a detailed outline of that proposed in [1] along with data obtained from simulations.

IV. Equal Timestamps or Low Density

It is convenient to divide our approach into two parts: first, how do we use the standard NRA's to efficiently do the gating type of matching in the straightforward case where the sensor reports have equal timestamps; and, second, how do we use these algorithms

for the case of unequal timestamps without acquiring an $O(N_t N_r)$ overhead, etc. As the gating problem is posed, it would be useful for the solution of the first part to calculate a search radius from a given score threshold. More specifically, in doing a search per report j on a track database, we need to determine the following: given a threshold, what is the radius squared, $r^2(threshold)$, such that all the report-track pairs which are separated by distances larger than $r^2(threshold)$ will not have scores above the threshold. Of course, for a one dimensional gaussian function with a fixed Γ , the function value is uniformly nonincreasing as r^2 increases, and falls below a threshold after r^2 gets larger than some value, say $r^2(threshold)$. It can be shown that it is possible to determine analytically an $r^2(threshold)$ that is independent of the Γ distribution and, furthermore, that a useful one can be found for $\beta > 1$ dimensions [6]. With such a solution and its obvious computational advantages, all pairs that are *candidate* for having scores within a threshold are found, using NRA's, by searching within a threshold radius.

Though the equal timestamp behavior of the near neighbors algorithm is straightforward enough, we include Plots 1 and 2 with data from the simulation. Plot 1 verifies the $O(N_t \ln N_t)$ CPU expense of creating the data structure to be searched. We have done the same simulation for two competing data structures, i.e. the OP and the BLD tree. Plot 2 verifies the search time scaling for the unequal timestamp case with "relatively small" difference in timestamp. Of course, any difference in timestamps will force a search with a larger radius than the case with no timestamp difference. Therefore, we consider this case to be an upper bound for the times and scaling of searching and scoring with equal timestamps. It is worthwhile to note the nearly ideal $O(N_r \ln N_t)$ search time scaling of the BLD tree, in Plot 2, in light of the fact that Plot 2 is for scenarios of fixed volume and both N_t and N_r were allowed to be as large as $32k$. That is, some scenarios were not exactly of very low object density and the BLD tree still performed very well.

V. High Density Unequal Timestamps: The Problem

When the reports have unequal timestamps what are the best times to which to integrate the tracks for making the potential pair matching? There are obvious answers if we are not concerned at all about efficiency; and also it is obviously easy - from the efficiency point of view - if we already know which report to pair with which track, but this is the problem we are trying to solve. It is possible to mishandle this task so that a combinatorial bottleneck will occur when matching. Assume we follow the textbook procedure of making the tracks one dataset valid at the beginning or end of the scan; and, also, that we use standard NRAs. Then the r^2 argument to the algorithms is not only dependent on error bounds from a score threshold, an $r^2(threshold)$ component, but also on bounds on positions determined by the location possibilities of the objects due to their dynamics and to the time differences. The latter factor can be orders of magnitude larger than the first. It is not difficult to imagine situations in which dynamics and object density will cause the near neighbors finding algorithms to return much of the data in the track dataset so that again we approach the $O(N_t N_r)$ scaling. And this horrendous scaling can occur not only for the score calculations, but also, in the neighbors finding section. This is so because the time of the NRAs' execution is dependent on the number of neighbors it returns, which in turn is dependent on r^2 , as will be argued later. In Plot 4 we have redone Plot 2 except that the scan length is

increased by a factor of five and therefore the average search radius is also increased. In this case neither of the two search algorithms scale as $O(N_r \ln N_i)$. The search times increased by a factor of about 2 and 5, for the OP and the BLD tree respectively, and the number of near neighbors returned was increased by a factor of about 10.

VI. High Density and Unequal Timestamps : Solution Description and Analysis.

Part of the motivation for our approach lies in the following observations: (1) that some data structures for NRAs are cheap to make - CPU wise, and (2) that by making various copies of the track data structure - the various copies valid at different times - a tradeoff can be made between the time spent on the creation of the data structures and the time spent on searching and scoring. The payoff from spending more time in creating data structures increases as the number and density increase and therefore may reduce the scaling of overall gating. Consider the case of a large number of objects with extremely high density and a scan length T_s , so that the r^2 argument to the NRA gives a search volume comparable in size to the extent of the object distribution. Also, suppose the object distribution is equally dense and random in each direction. Then, naturally, many if not all objects will be returned as candidates by the NRA and we are near the $O(N_i N_r)$ scaling that we want to avoid.

If we make N_i track data structures with NRAs valid at N_i equally spaced time intervals within the scan of length T_s , then any report would be at most $T_s/(2N_i)$ time units away from a track data structure (TDS). The average radius to the NRA is decreased by the factor N_i - compared to the case where we have one copy at the *middle* of the scantime - and the volume extent as well as the average number of candidates returned is smaller by $(1/N_i)^3$ in the isotropic dense limit 3D case. That is, in this limit the total number of N objects in N_r spheres each of radius $r_i = iV_{max}T_s/N_i^{1/3}$ is given by

$$N = \rho \left(\frac{4\pi}{3}\right) 2N_i \sum_{i=1}^{N_r/2N_i} \left(i \frac{V_{max}T_s}{N_i^{1/3}}\right)^3 \quad (2)$$

where ρ is the track density and V_{max} is the speed. The sum has an exact solution as a function of N_r , but in the large N_r limit we have

$$N = \rho(4\pi/3)2N_i(V_{max}T_s/N_i^{1/3})^3 \left(\frac{1}{3+1}\right) \left(\frac{N_r}{2N_i}\right)^{3+1} \quad (3)$$

and for a fixed N_i , N_r and T_s , then:

$$N \propto (1/N_i)^3 \quad (4)$$

Overall CPU time could be reduced since scoring time is directly proportional to the number of near neighbors found as is searching time - though exactly how depends on the particular NRA. Though our simulation is somewhat degenerate in one of the 3 space dimensions, for only 32K objects and $T_s = 10s$, the number of near neighbors returned decreased by an average factor of 9.8 when N_i was changed from 1 to 5. Also,

for $N_i = 5$, the number of near neighbors returned was decreased by a factor of 62.7 compared to the case of 1 TDS placed at the beginning of the scan. Plot 5 shows how the scaling of the search time behaves for the same scenario as in Plot 4, except that now $N_i = 5$ for the datasets of 4K and 32K tracks. The best fit lines approach the $N \ln N$ scaling line more closely. Also, for the same runs, Plot 5 shows that with multiple copies the scaling for scoring was less than $O(N \ln N)$, and the data shows it was almost linear. Of course, a price was paid in creation of the multiple copies and data structures.

Was the price paid for the multiple data copies too high so that the overall cost would still scale worse than $N \ln N$? Let k be the average number of near neighbors returned. Then the total CPU cost can be modeled as

$$T(N_t, N_r, N_i, k,) = C_1 N_i N_t + C_2 N_i N_t \ln N_t + (C_{3a} N_r \ln N_t + C_{3b} N_r k) + C_4 k N_r \quad (5)$$

where the terms on the right hand side of equation (5) give respectively, the cost for integrating the tracks to the desired time of the data structures, the cost of making the data structures (BLD tree case), the cost of searching the appropriate data structure for each report (BLD tree case), and the cost of scoring the pairs. Of course, k is a function of the density and the total volume searched:

$$k = k(\rho, r^2). \quad (6)$$

where $\rho = \rho(N_t, Vol)$ and $r^2 = r^2(T_s, N_i, \Gamma, V_{max})$. In the case of constant volume - the case we actually modeled - a fixed T_s , dense and isotropic and in which Γ provides a correction to r of lower order than that determined by the dynamics, then

$$k \propto k(N_t, N_i) \propto N_t / (N_i^\beta). \quad (7)$$

Now we can rewrite equation (5) as

$$T(N_r, N_t, N_i) = C_1 N_i N_t + C_2 N_i N_t \ln N_t + C_{3a} N_r \ln N_t + C_{3b} N_r \left(\frac{N_t}{N_i^\beta} \right) + C_4 N_r \left(\frac{N_t}{N_i^\beta} \right). \quad (8)$$

The function above has a minimum, which can be verified to be

$$N_{i_{min}} = (\beta N_r (C_{3b} + C_4)) / (C_1 + C_2 \ln N_t)^{(1/(\beta+1))} \quad (9)$$

and substituting equation (9) into (8) we find an upper bound on the leading scaling term goes as $O(N_t \ln N_t N_r^{1/(\beta+1)})$. Of course, with random timestamps within a scan, only in the assumed dense limit will it scale this poorly as compared to the $N_r \ln N_t$ scaling of the low density case.

VII. Discussion

Not only is the value of N_i , for a given N_t and N_r , software dependent, but it is also dependent on the computer used. For example a vector computer with good floating point hardware will no doubt reduce C_4 , over a generic computer, but because C_1 can be reduced by an even larger factor since vectorization of the integration of the equations of motion will be straightforward and possibly complete. Thus the values of the constants will need to be "in house empirical" in every hardware/software setup.

Because only scaling data was provided, we should mention that the code currently takes about 1 minute on a Sun 3/260 to process a case in which $N_t = N_r = 4K$. By processing we mean the time to generate all the data and to find and score the candidates twice - once for each NRA.

VIII. Conclusion

In this paper we have presented an efficient approach to gating in multitarget tracking. A technique was presented to (1) handle the case of fixed object density, or sufficiently low density, with equal or nearly equal observation timestamps, and (2) to handle the case of high density with observation reports of unequal timestamps. For the former case we verified that the overall cost of making observation-track pairs scale as $O(N_r \ln N_t)$. For the latter case we showed that the overall cost of making the pairs can be made to scale better than $N_t \ln N_t N_r^{(1/(\beta+1))}$. In both cases we used "near-neighbors-within-a-radius" search algorithms, and in the latter case we introduced a new auxiliary algorithm to achieve the stated gating.

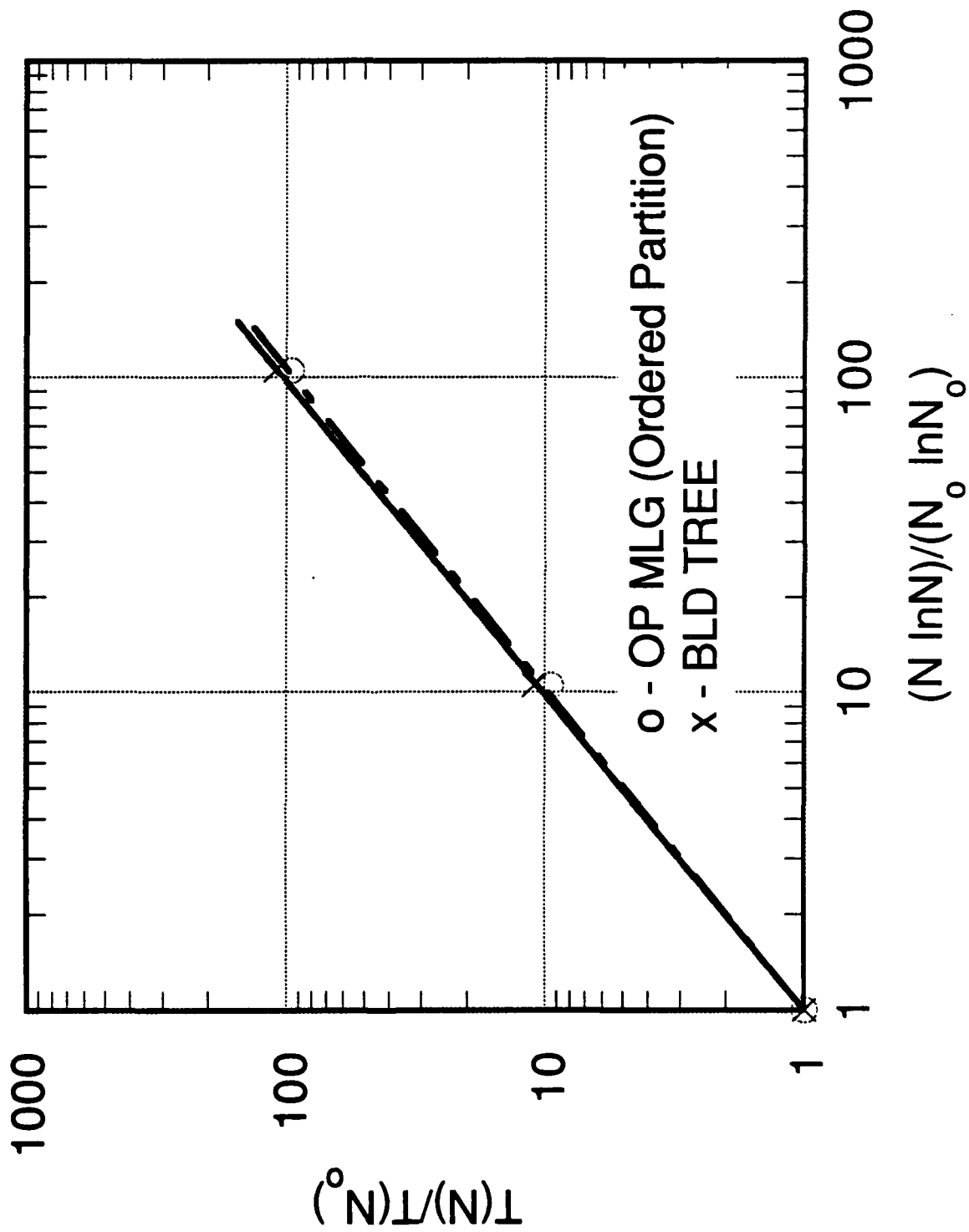
Acknowledgements I would like to thank Dr. J. Michael Picone for his helpful discussions on the problems treated here, and Dr. Ellis Hyman for his considerable editorial guidance. This work was performed under US N.R.L. contract No. N00014-86-C-2197

References

- [1] E. Hyman, S. Eidelman, M. Zuniga, and M. Redmon: "Numerical Modeling of Airblast, Second Year Annual Report." *SAIC Report No. 88/1779,3 (1988)*.
- [2] S.S. Blackman: Multiple-Target Tracking with Radar Applications, Artech House, Dedham, MA, 1986.
- [3] R.P. Wishner, F.X. Lanzinger, H.M. Mesiwala, and S. Mori, "Advanced Techniques for Multi-Target Track Formation.", Advanced Information and Decision Systems, Mountain View, CA, 1981.
- [4] Jeff Uhlmann, "A Remedy for The Hierarchical Divisibility Problem Using A Bilinear Decomposition.", Berkeley Research Associates Report No. BRA-89-W040R, Berkeley, CA, June 1989.
- [5] Kim, Baek S., Park, Song B., "A Fast k Nearest Neighbor Finding Algorithm Based on the Ordered Partition." *IEEE Vol. PAMI-8*, No. 6, Nov. 1986.
- [6] J.M. Picone, M. Zuniga, J. Uhlmann, To be published (1989).

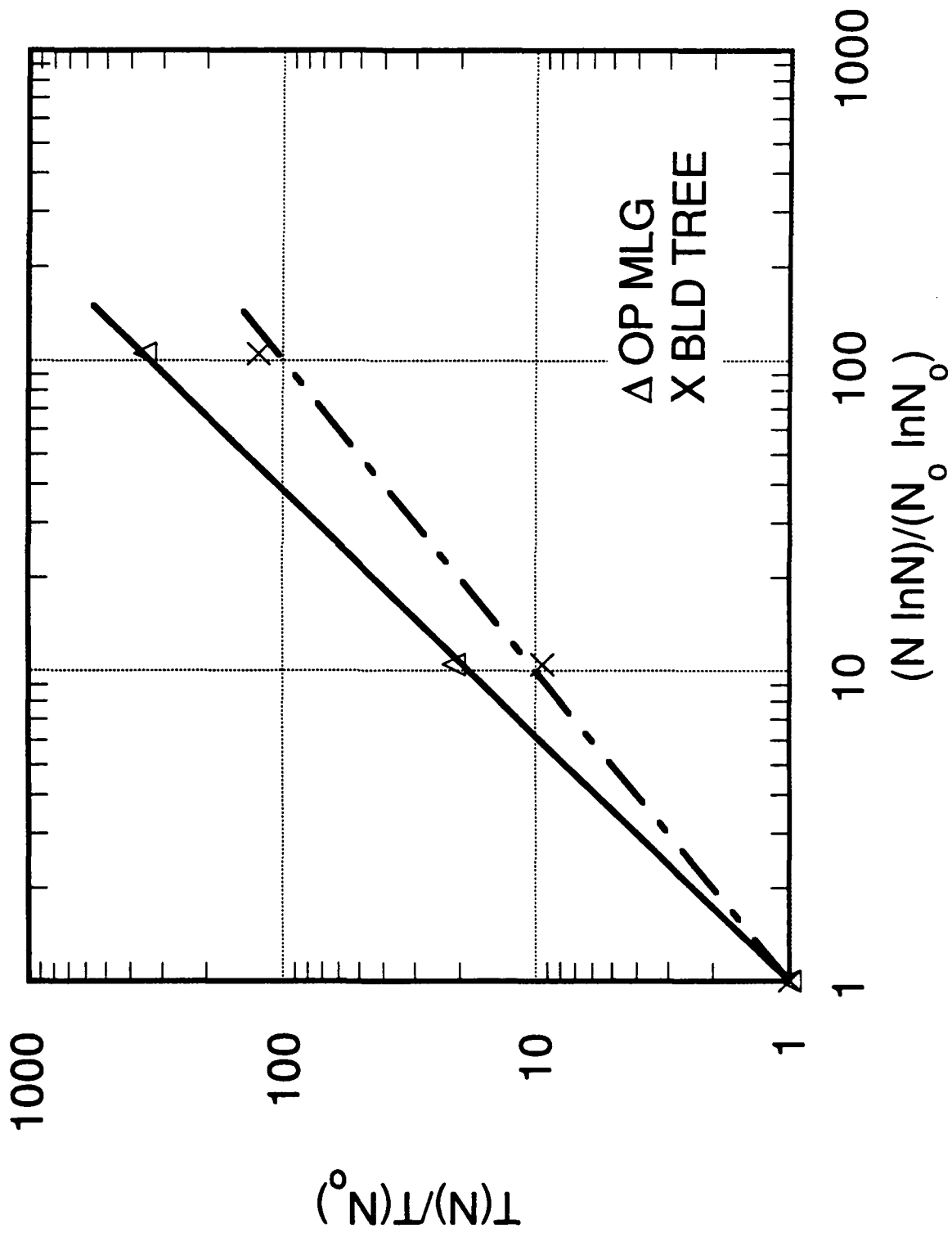
Plot 1

Make times scaling of search structures.



Plot 2

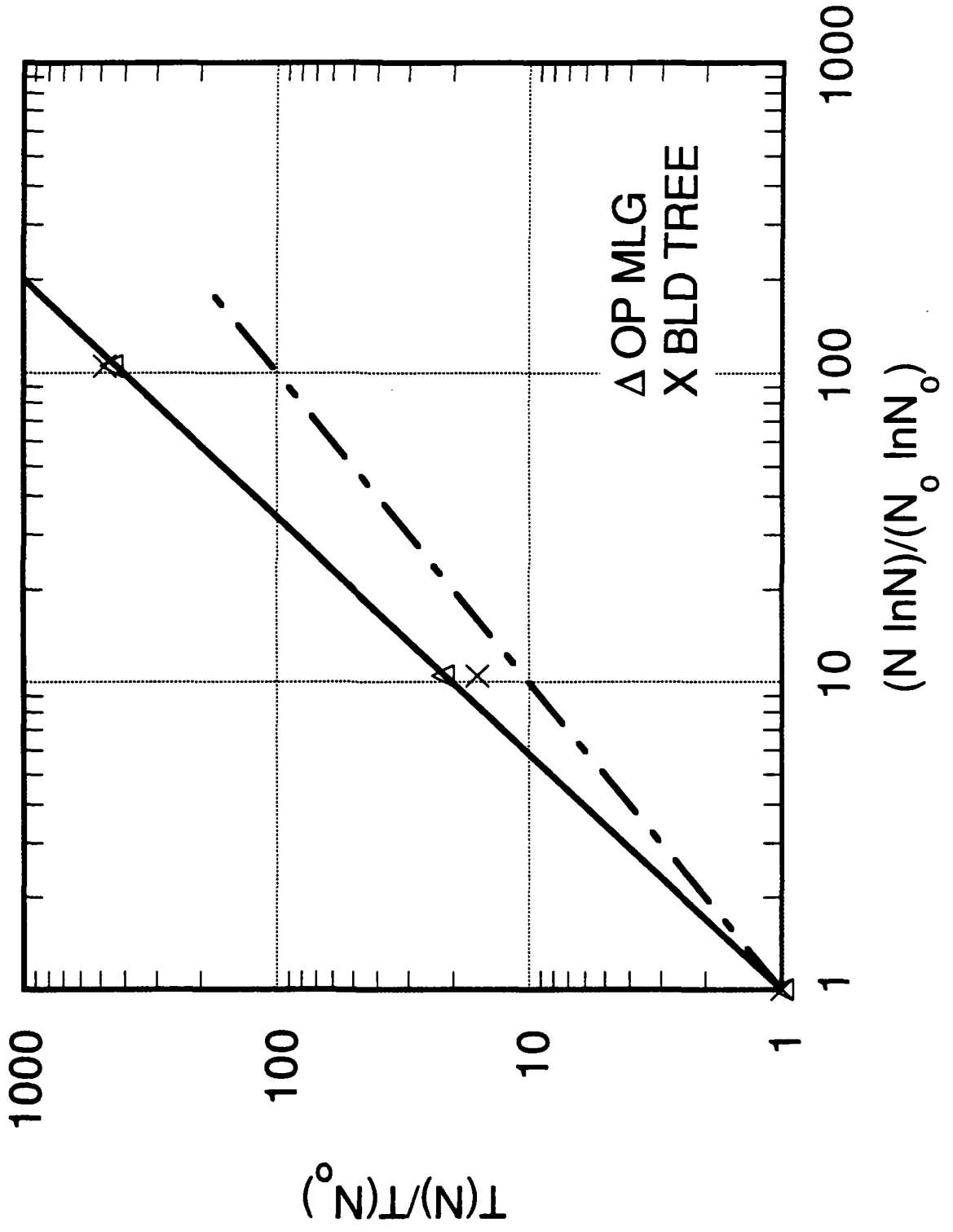
Search Time Scaling of Data Structures. Search for neighbors of N reports among data structures with N tracks; return Pairs.



Plot 4

Search time scaling.

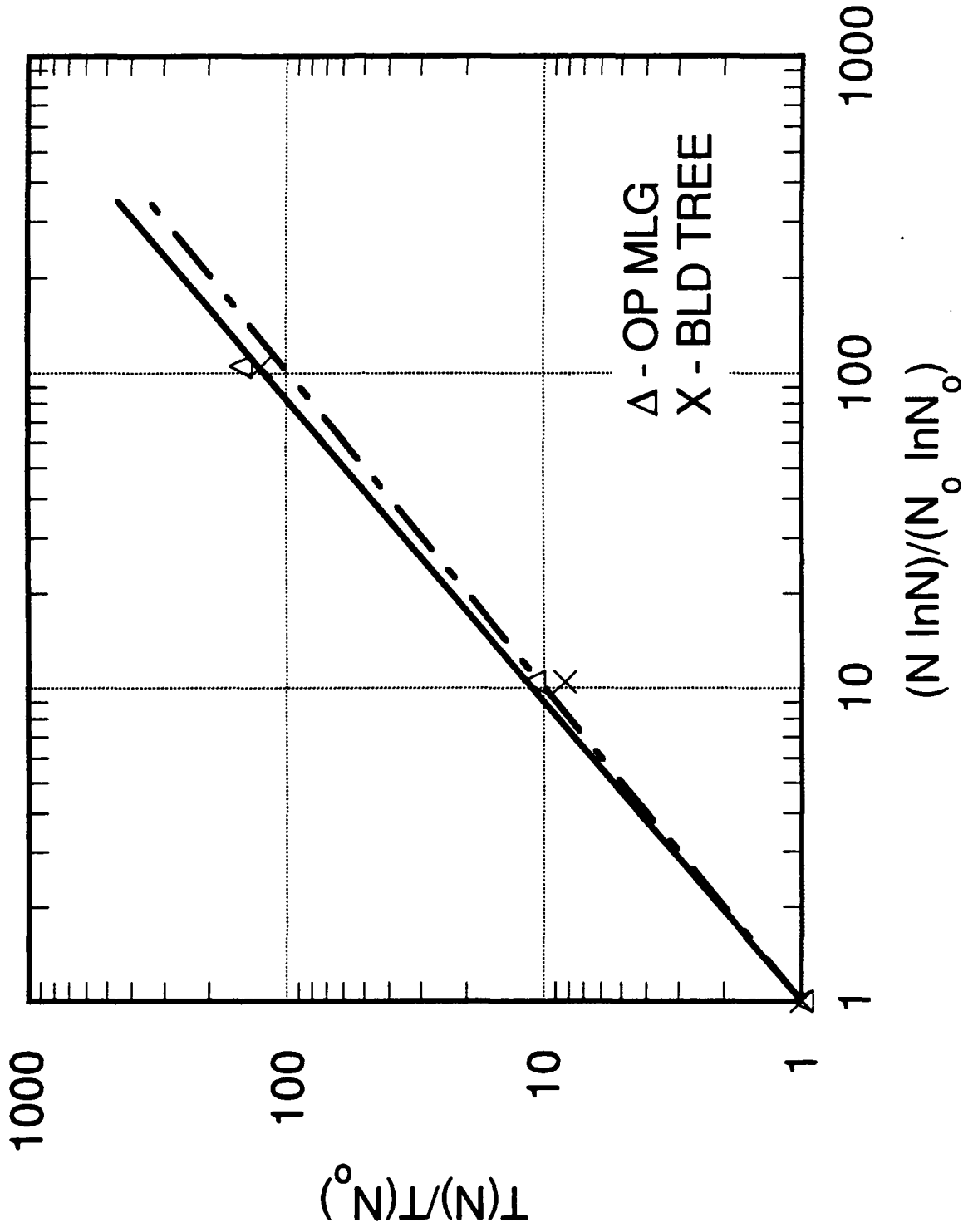
TS = 10 sec; 1 copy of track structure.



Plot 5

Search time scaling. Multiple track data copies.

TS = 10 sec.; 1 copy for N = 512; 5 copies for N = 4K and 32K.



Plot 6

Scoring scaling, or scaling of # neighbor tracks found.
TS = 10 sec.

